IPP-Report

Max-Planck-Institut
für Plasmaphysik

Verena Mitterauer

Non-linear simulations of the penetration of error fields into tokamak plasmas

IPP 2021-16
Oktober 2021

Technische Universität München
Fakultät für Physik

Abschlussarbeit im Masterstudiengang Physik

Non-linear simulations of the penetration of error fields into tokamak plasmas

Verena Mitterauer

1. Juni 2021

Erstgutachterin: Prof. Dr. Sibylle Günter
Zweitgutachter: Dr. Stefan Recksiegel
Betreuer: Dr. Matthias Hölzl

durchgeführt am Max-Planck-Institut für Plasmaphysik, Garching bei München

Contents

Motivation

The development of a nuclear fusion power plant is an ambitious project with the goal to contribute to the world's rising energy demands in a clean and sustainable way. Substantial progress has been made in the last decades, and multiple designs for fusion reactors have been conceived. To this date, the most advanced type is the tokamak, a toroidal vacuum chamber equipped with strong magnetic coils. It uses magnetic fields to trap plasma, a highly ionized, low-density gas, of temperatures so high that no material wall could withstand prolonged contact. The plasma, often consisting of hydrogen isotopes, is the fuel for nuclear fusion reactions. When two fuel ions collide, their high thermal energy may cause them to fuse into heavier particles. In this process, part of their binding energy is converted into kinetic energy, which can be harnessed and used to generate electricity.

However, before the commercial operation of a tokamak is conceivable, a number of challenges have to be addressed, one of which is the plasma stability. In order to reach the high core temperatures, the particles have to be confined extremely well within the magnetic fields. The operation in the so-called high confinement mode, or H-Mode, is therefore favorable. This operational mode comes with a narrow region of strongly reduced particle and heat transport, which is located close to the edge of the plasma near the wall of the tokamak. The transport barrier establishes a steep pressure gradient at the edge, which can drive plasma instabilities in the region. The consequence is the onset of repeated violent expulsions of heat and particles from the plasma to the wall of the tokamak, known as Edge Localized Modes (ELMs). ELMs are a concern for ITER, the worlds largest tokamak, which is currently under construction in the south of France. Due to its large plasma volume the heat load of large ELMs could severely reduce the lifetime of the materials in the so-called divertor region. Considerable effort within the fusion community is therefore dedicated to the development of ELM control mechanisms, among which is the application of small non-axisymmetric magnetic fields by external coils, known as Resonant Magnetic Perturbations (RMPs). Despite the fact that RMP ELM control has been demonstrated in various tokamaks, the physical mechanisms are still subject to active research and the extrapolation to ITER still has considerable uncertainties.

An important contribution to the physics understanding of RMPs comes from modeling. Numerous codes have been developed to simulate different aspects of RMP physics. Among them is the code JOREK [1], which is used for the studies carried

out in this thesis. JOREK solves the reduced MHD equations, which describe the behavior of the plasma as a single, conducting fluid, in realistic tokamak geometries. The equations are discretized by a Bézier finite element grid in the 2D poloidal plane, combined with a Fourier expansion in toroidal direction [2]. Dirichlet boundary conditions are used for most variables, which force the values at the boundary to be constant in time. Physically this corresponds to the effect of an ideally conductive wall close to the plasma.

The JOREK code can be combined with its free boundary extension STARWALL [3]. STARWALL calculates the effect of conductive structures surrounding the plasma and provides the relevant information to JOREK [4]. This makes it possible to use natural boundary conditions, where the ideally conducting wall is replaced by the effect of realistic structures.

In previous years JOREK (without the STARWALL extension) has been used extensively to model both ELMs [5–7] and RMPs [8, 9], as well as the RMP-ELM interaction [10–13], including RMP-ELM control. By using JOREK-STARWALL the RMP-ELM modeling can be improved further, as the perturbation fields can evolve freely on the boundary.

The goal of this thesis is to carry out first-of-a-kind free boundary RMP simulations using JOREK-STARWALL. For this purpose, the implementation of the RMP coils in STARWALL is corrected and tested. The validation confirms that the coils can be used reliably for RMP studies. Then, the penetration of RMPs into an ASDEX Upgrade H-Mode plasma is simulated using free boundary conditions. The analysis of the results shows a good qualitative agreement with the theoretical expectations. A subsequent comparison to simulations, where fixed boundary conditions are applied, reveals that the boundary conditions have an impact on the response of the plasma to the RMPs. Lastly, the onset of a type-I ELM is simulated with free boundary conditions. It is shown that in the absence of the effects of an ideal wall the stability limits are lowered, which leads to an earlier ELM onset at lower pedestal pressure gradients. Both the RMP penetration studies, as well as the ELM simulations, open up many interesting questions for future investigations.

The thesis is structured as follows: In part I an overview of the main principles of fusion research (chapter 1), magnetic confinement fusion (chapter 2) and resonant magnetic perturbations (chapter 3) is given. Furthermore, the JOREK-STARWALL code is introduced in chapter 4. Part II presents the results of the modeling studies that were carried out for this thesis. The validation of the RMP coils in STARWALL is presented in chapter 5. The first JOREK-STARWALL free boundary RMP simulations are discussed in chapter 6, which is followed by the comparison to their fixed boundary equivalent in chapter 7. Lastly, the ELM studies are discussed in chapter 8.

Part I

Theoretical Background

Chapter 1

Fusion research

Nuclear fusion occurs if two ions collide with sufficient energy, so that the distance between their nuclei becomes small enough for the strong nuclear force to outweigh the repulsive Coulomb potential. As a consequence, the particles combine and form heavier nuclei. In the case of light reactant nuclei fusion is generally releasing energy in the form of kinetic energy, which originates from the difference in the binding energy between the reactants and the products.

At present day, the reaction that is the easiest to exploit on earth is the fusion of deuterium (D) and tritium (T) into an alpha particle (He), a neutron (n) and 17.59 MeV of kinetic energy, of which the neutron carries 14.03 MeV and the helium-nucleus carries 3.56 MeV.

$$\mathrm{D} + \mathrm{T} \rightarrow \mathrm{He} + \mathrm{n} + 17.59\ \mathrm{MeV} \tag{1.1}$$

The advantage of the D-T reaction is its high *reaction cross-section* σ at relatively low temperatures compared to other fusion reactions. The cross section quantifies the probability of a fusion reaction to occur and it is dependent on the relative velocity between the two particles, i.e. their kinetic energy. Figure 1.1 shows the energy dependency of the cross section for different fusion reactions. For the D-T fusion the cross section peaks at around 20 - 70 keV, at a far lower energy and higher value than other fusion reactions.

At energies where fusion is likely to occur, the kinetic energy of the fuel particles is higher than their ionization energy. Therefore, the fuel mixture is almost completely ionized, and reacts to electromagnetic fields differently than a regular gas. An especially important property follows from the high mobility of the electrons and ions, which may lead to a very efficient screening of externally applied fields. If the system is overall electrically neutral, and charged regions only appear on scales much smaller than the system size, the so-called *quasi-neutrality* condition is fulfilled. A highly ionized and quasi-neutral gas is referred to as *plasma*.

The velocity distribution of the particles in a plasma, along with the cross section σ, determines the rate at which fusion reactions occur. The number of fusion reactions per time and unit volume is obtained by averaging over these two properties $\langle \sigma(v)v \rangle$.

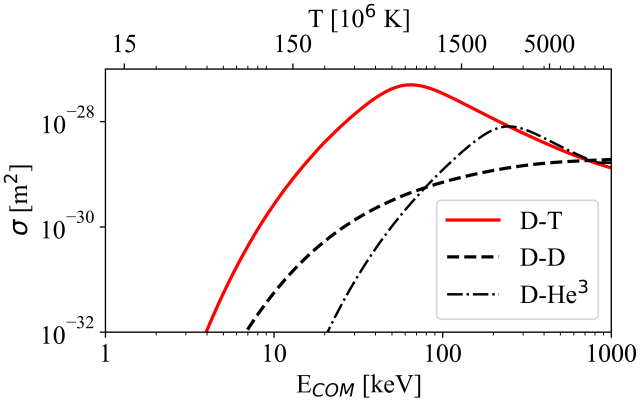

Figure 1.1: Cross sections σ of the Deuterium-Tritium (D-T), Deuterium-Deuterium (D-D) and Deuterium-Helium3 (D-He^3 fusion reactions as a function of temperature T and center-of-mass Energy E_{COM}. The D-T fusion is favorable due to its high reaction cross section at low temperatures. (data from [14])

From the reaction rate the total power generated by fusion processes P_{fusion} in a D-T plasma can be determined

$$P_{\text{fusion}} = n_D \; n_T \; \langle \sigma(v) v \rangle \; E_{\text{fusion}}. \tag{1.2}$$

Here, n_D and n_T are the particle densities of deuterium and tritium respectively, and $E_{\text{fusion}} = 17.59$ MeV is the generated energy per D-T fusion reaction. The maximum reaction rate is obtained for $n_D = n_T = \frac{1}{2}$ n, when Deuterium and Tritium are present in equal parts.

Naturally, an economically viable fusion reactor should aim at a high P_{fusion}, while at the same time minimizing the external energy P_{heat} that is needed to heat the plasma. The ratio between output and input energy, called *amplification factor* Q, is therefore an important figure of merit for the efficiency of a fusion reactor

$$Q = \frac{P_{\text{fusion}}}{P_{\text{heat}}} \tag{1.3}$$

The highest Q attained in a fusion experiment so far was about Q ≈ 0.64 in the nuclear fusion reactor JET. At Q $= 1$ the so-called "break-even" condition would be reached, where the fusion power balances the external heating power exactly. An important limit for a fusion reactor is the *ignition state*, which is enabled by the self-heating properties of the plasma. The D-T fusion generates alpha particles, which carry about a fifth of the energy of the fusion reaction. The energy can be transferred to the D-T fuel and thereby heat it. If enough alpha particles are generated, so that the energy they provide compensates all occurring energy losses, no external heating

power needs to be injected. At this Q = ∞ state, a *burning plasma* is achieved. In practice, a reactor would still operate at a finite Q to simplify control.

The energy loss in a fusion device is quantified by the *energy confinement time* τ_E

$$\tau_E = \frac{W}{P_{loss}} \tag{1.4}$$

It corresponds to the characteristic time that it takes for a plasma to cool down if all external heating is turned off. Taking $W \approx 3V\bar{n}\bar{T}$ as an estimate for the thermal plasma energy, and $P_\alpha = \frac{1}{5}P_{\text{fusion}} \geq P_{\text{loss}}$ as requirement for ignition, one can derive

$$\bar{n}\ \bar{T}\ \tau_E \geq 1.5 \times 10^{20}\,\text{m}^{-3}\text{keVs} \tag{1.5}$$

as an ignition condition for a pure D-T plasma with $\bar{n} = \frac{1}{2}\bar{n}_D = \frac{1}{2}\bar{n}_T$ as average plasma density and $\bar{T}$ as average plasma temperature. This form of the ignition condition is called *Lawson criterion*. The product of $\bar{n}\ \bar{T}\ \tau_E$ on the left hand side is called *triple product*, and it is considered another important figure of merit in fusion research.

On earth the Lawson criterion may be fulfilled by two very different approaches. In *inertial confinement fusion*, the plasma particles are "confined" only for the time of their acceleration. The very short energy confinement times ($\tau_E \approx 10^{-11}\ s$) are balanced by extremely high plasma densities ($n \approx 10^{31}\ \text{m}^{-3}$).

The second approach is *magnetic confinement fusion*, where strong magnetic fields are responsible for confining the plasma particles. Compared to inertial confinement fusion, the energy confinement time is considerably longer, which allows for lower plasma densities ($n \approx 10^{20}\ \text{m}^{-3}$). This thesis will only focus on magnetic confinement fusion, with the tokamak as fusion device.

Chapter 2

Magnetic Confinement Fusion

Magnetic confinement fusion aims at creating a macroscopically stable plasma with high energy confinement times by using magnetic fields. To achieve this goal, a framework has to be found, that allows to describe the behavior of plasma particles in a magnetic field. Throughout the decades, different descriptions have been developed. To study the large scale phenomena of interest in this thesis Magnetohydrodynamics (MHD) poses a suitable framework. The principles of MHD are introduced based on ideal MHD in section 2.1. This simplest version of the MHD model is sufficient to discuss some of the basic principles of a magnetic confinement device: the requirements concerning the magnetic field configuration (section 2.2), the design (section 2.3) and some of the challenges (section 2.4). A more advanced MHD picture, that is necessary for accurate simulations, is presented at a later time together with the computational framework.

The contents of this chapter summarize the derivations found in popular plasma physics textbooks [15, 16].

2.1 Ideal MHD

The description of the behavior of a plasma by the equations of motions of the N plasma particles requires a 6N-dimensional coupled system of equations. Typically N is of the order of 10^{20}, which makes such a system practically impossible to solve on any reasonable timescale. An alternative description is provided by the MHD model. Instead of determining the location and momentum of each individual particle, one uses macroscopic statistical quantities to define the state of the system. The treatment of the plasma as a fluid does not only lower the computational cost, but it has the additional advantage that the macroscopic statistical quantities are directly measurable in experiment. Because MHD equations, and even more so ideal MHD equations, rely on assumptions about the plasma state, care has to be taken that the phenomena of interest lie within the range of validity of the selected model. The derivation of the ideal MHD equations is only outlined here, thorough derivations can be found in [15, 16]

For the transition from the 6N-dimensional system of equations to the fluid picture it is helpful to first introduce the distribution function $f_s(\boldsymbol{x}, \boldsymbol{v}, t)$, which gives the number of particles of species s (either electrons e or ions i) with velocity $\boldsymbol{v}$ at location $\boldsymbol{x}$ and time t. It is a more convenient description of the system without loss of information, since within each species the particles are indistinguishable.

The time evolution of the distribution function is described by the kinetic equation. It is the equivalent of the Boltzmann equation for kinetic particles, but adapted to the case of a plasma. It is given by

$$\frac{\partial}{\partial t} f_s(\boldsymbol{x}, \boldsymbol{v}) + \boldsymbol{v} \cdot \nabla f_s(\boldsymbol{x}, \boldsymbol{v}) + \frac{q}{m}(\boldsymbol{E} + \boldsymbol{v} \times \boldsymbol{B}) \cdot \nabla_v f_s(\boldsymbol{x}, \boldsymbol{v}) = \left(\frac{\partial f_s(\boldsymbol{x}, \boldsymbol{v})}{\partial t} \right)_{coll.} \quad (2.1)$$

The second term on the l.h.s. corresponds to the effects of particle convection, while the third term on the l.h.s. describes the forces acting on the particles. The force term depends on the fields $\boldsymbol{E}$ and $\boldsymbol{B}$, which are collectively and self-consistently generated by the particles. For this reason, the complete system is obtained by the coupling to the Maxwell equations. The term on the right hand side is the particle collision operator. It is not explicitly given here, as in general it can take on various forms depending on the system.

The fluid description uses macroscopic statistical quantities, which are derived from the lowest order velocity moments $M_k(\boldsymbol{x}, t)$ of the distribution function. The velocity moments have the form $M_k(\boldsymbol{x}, t) = \int \boldsymbol{v}\boldsymbol{v}..\boldsymbol{v} f_s(\boldsymbol{x}, \boldsymbol{v}, t) d^3v$ with k factors of $\boldsymbol{v}$:

particle number density
$$n_s(\boldsymbol{x}, t) = \int f_s(\boldsymbol{x}, \boldsymbol{v}, t) d^3v, \quad (2.2)$$

particle flux density
$$n_s \boldsymbol{u_s}(\boldsymbol{r}, t) = \int v f_s(\boldsymbol{x}, \boldsymbol{v}, t) d^3v, \quad (2.3)$$

pressure tensor
$$\underline{p}_s(\boldsymbol{r}, t) = \int m_s \boldsymbol{w_s} \boldsymbol{w_s} f_s(\boldsymbol{x}, \boldsymbol{v}, t) d^3v, \quad (2.4)$$

heat flux density
$$\underline{q}_s(\boldsymbol{r}, t) = \int m_s w_s^2 \boldsymbol{w_s} f_s(\boldsymbol{x}, \boldsymbol{v}, t) d^3v \quad (2.5)$$

The particle flux density is used to define the flow velocity $\boldsymbol{u_s}(\boldsymbol{r}, t)$. The pressure tensor and the heat flux density are expressed in their more commonly used form in the rest frame of the species, with the relative velocity $\boldsymbol{w_s} \equiv \boldsymbol{v} - \boldsymbol{u_s}$. m_s denotes the mass of the species. In addition, some derived quantities can be defined for convenience. The *charge density* is given by $\rho_s = e_s n_s$, where e_s is the species charge. The trace of the pressure tensor gives the scalar *pressure* $p_s \equiv \frac{1}{3} Tr(\underline{p}_s)$, which in turn is used to define the *temperature* of a plasma in a thermodynamic equilibrium $T_s \equiv \frac{p_s}{n_s}$.

The time evolution of the macroscopic quantities is obtained by taking the lowest velocity moments of the kinetic equation. By using the notation $m_k = \boldsymbol{v}\boldsymbol{v}\boldsymbol{v}...\boldsymbol{v}$ with

k factors of $\boldsymbol{v}$, the k-th moment of the kinetic equation can be given in a general form. m_k can both be a scalar and a vector, it is written in scalar notation here.

$$\frac{\partial}{\partial t}\int m_k f_s d^3v_s + \nabla \int \boldsymbol{v_s} m_k f_s d^3v_s - m_s \int (\boldsymbol{F}\nabla_v) m_k f_s d^3v_s = \int m_k f_s \left(\frac{\partial f}{\partial t}\right)_{coll.} d^3v_s \tag{2.6}$$

The factor $\int \boldsymbol{v} m_k f d^3v$ in the second term on the left hand side corresponds to the next highest order moment. Its appearance indicates that each conservation equation depends on the next highest moment and its corresponding conservation equation. This means it is impossible to obtain a closed system of equations just from the moment expansion. At some point, the expansion has to be truncated and a suitable closure has to be found, which requires an assumption about the system. A frequently used choice is to assume an adiabatic plasma. With this closure, and taking the plasma to consist of one ion species and electrons, the two-fluid equations can be derived. They are found in [15].

A further simplification of the two-fluid model leads to the MHD model, where the plasma is treated as a single, electrically conductive fluid. The MHD quantities (density ρ, one fluid flow velocity $\boldsymbol{v}$, current density $\boldsymbol{j}$ and pressure p) are obtained by combining the two-fluid quantities.

$$\rho = m_i n_i + m_e n_e \approx m_i n_i \tag{2.7}$$

$$\boldsymbol{v} = \frac{1}{\rho}(m_i n_i \boldsymbol{u_i} + m_e n_e \boldsymbol{u_e}) \approx u_i \tag{2.8}$$

$$\boldsymbol{j} = en(\boldsymbol{u_i} - \boldsymbol{u_e}) \tag{2.9}$$

$$p = p_i + p_e \tag{2.10}$$

For the derivation of equations (2.7) and (2.8), the electron mass m_e is neglected ($m_i \gg m_e$) and the quasi-neutrality condition $\mathrm{n}_e = \mathrm{n}_i = \mathrm{n}$ is used.

The derivation of the MHD equations from the two fluid equations can be found in [15]. Different versions of the MHD equations can be derived, with varying validity ranges depending on the assumptions made during the derivation. The simplest

MHD picture is given by the set of *ideal MHD equations*:

$$\frac{\partial \rho}{\partial t} + \nabla(\rho \boldsymbol{v}) = 0 \qquad \text{continuity equation} \quad (2.11)$$

$$\rho \left(\frac{\partial}{\partial t} + \boldsymbol{v} \cdot \nabla \right) \boldsymbol{v} = \boldsymbol{j} \times \boldsymbol{B} - \nabla p \qquad \text{momentum equation} \quad (2.12)$$

$$\boldsymbol{E} + \boldsymbol{v} \times \boldsymbol{B} = 0 \qquad \text{Ohm's law} \quad (2.13)$$

$$\nabla \times \boldsymbol{E} = -\frac{\partial \boldsymbol{B}}{\partial t} \qquad \text{Faraday's law} \quad (2.14)$$

$$\nabla \times \boldsymbol{B} = \mu_0 \boldsymbol{j} \qquad \text{Ampère's law} \quad (2.15)$$

$$\nabla \cdot \boldsymbol{B} = 0 \qquad \text{magnetic divergence constraint} \quad (2.16)$$

$$\frac{d}{dt} \left(\frac{p}{\rho^\gamma} \right) = 0 \qquad \text{adiabatic equation of state} \quad (2.17)$$

If the plasma resistivity σ is taken into account, Ohm's Law (equation 2.13) is replaced by its resistive equivalent $\sigma(\boldsymbol{E} + \boldsymbol{v} \times \boldsymbol{B}) = \boldsymbol{j}$. The set of equations is then referred to as *resistive MHD*.

The MHD equations are applicable if, in addition to the earlier discussed assumptions to quasi-neutrality, resistivity and electron mass, certain conditions are fulfilled. The plasma is assumed to be strongly magnetized, so that the ion Larmor radius is smaller than the length scales of interest. Furthermore, the mean free path between collisions is assumed to be small compared to typical gradient scales $|\nabla f|/f$ appearing in the plasma, so that the high collisionality ensures that the system is in a local thermodynamic equilibrium.

Despite the fact that fusion plasmas may lie outside this formal range of validity, the MHD equations have been found to provide a surprisingly good description of some aspects of the plasma behavior.

2.2 Equilibrium

Ideal MHD is a suitable framework to examine which magnetic field configurations can be expected to confine the plasma particles well. A basic condition for long confinement times is that the plasma is held in an equilibrium, where $\frac{d}{dt} = 0$ for all quantities. For now we will assume the equilibrium to be static with $\boldsymbol{v} = 0$. Applying this condition to the ideal MHD equation yields the criteria for an equilibrium magnetic field configuration.

$$\nabla p = \boldsymbol{j} \times \boldsymbol{B} \quad (2.18)$$

$$\nabla \times \boldsymbol{B} = \mu_0 \boldsymbol{j} \quad (2.19)$$

$$\nabla \cdot \boldsymbol{B} = 0 \quad (2.20)$$

A general property of the equilibrium can be derived from equation 2.18. From taking the dot product with $\boldsymbol{B}$ it follows that $\boldsymbol{B} \cdot \nabla p = 0$, which implies that the pressure along the field lines is constant.

This result is a reflection of the fact that the plasma moves freely parallel to the field lines. Long confinement times are therefore more easily achieved, when the field lines are not intersecting with material walls. This is the case for toroidal field configurations, which are commonly used in magnetic confinement fusion.

2.2.1 Grad-Shafranov equation

If the configuration is not only toroidal but also axisymmetric the equilibrium problem can be reformulated in a particularly simple way [16]. Because of the axisymmetry and $\nabla \cdot \boldsymbol{B} = 0$ the magnetic field can be expressed in terms of a stream function $\boldsymbol{\Psi}$. Ampères Law (equation 2.15) is used to also rewrite the current density $\boldsymbol{j}$ in terms of $\boldsymbol{\Psi}$. By introducing two free functions $F^2(\Psi)$ and $p(\Psi)$ the 3D equilibrium conditions can then be reduced to a single equation that only depends on the stream function. This is the so-called *Grad-Shafranov equation* [17], given in cylindrical coordinates (R, Z, ϕ)

$$R\frac{\partial}{\partial R}(\frac{1}{R}\frac{\partial}{\partial R}\Psi) + \frac{\partial^2}{\partial Z^2}\Psi = -\mu_0 R^2 \frac{dp}{d\Psi} - \frac{dF^2}{d\Psi}. \tag{2.21}$$

The Grad-Shafranov equation defines the magnetic equilibrium by the choice of $F^2(\Psi)$ and $p(\Psi)$ together with appropriate boundary conditions. The stream function is related to the physical poloidal magnetic flux $\Psi = \frac{1}{2\pi}\int \boldsymbol{B} d\boldsymbol{S}$.

A solution to the Grad-Shafranov equation is schematically illustrated in figure 2.1. The magnetic field is arranged in nested toroidal surfaces. A field line that lies on a particular surface stays on that same surface and helically winds around the torus. The magnetic flux that passes through any cross-section of one surface is constant. The nested surfaces are therefore given the name flux surfaces. Since the pressure has been found to be constant along the field lines the flux surfaces are also isobaric.

The inclination of the helically winding field lines is described by the *safety factor* q, the ratio between their change in toroidal direction and their change in poloidal direction:

$$q(r) = \frac{d\phi}{d\theta}. \tag{2.22}$$

On surfaces with a rational q value ($q = m/n$) the field lines close in on themselves after n toroidal and m poloidal turns. These so-called rational surfaces are sensitive to perturbations to the equilibrium.

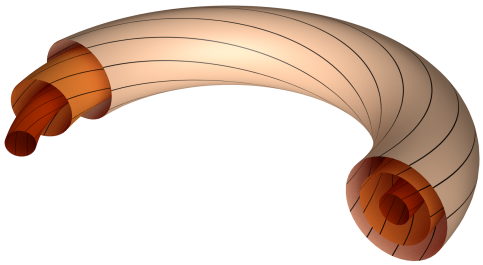

Figure 2.1: In one of the solutions of the Grad-Shafranov equation, the field line are arranged on nested toroidal surfaces. (own figure)

2.2.2 Flux coordinates

Instead of the use of cylindrical coordinates, the toroidal geometry of the problems in fusion research makes the use of the toroidal coordinate system (r, θ, ϕ) often more convenient. Here r is the minor radius, θ is the poloidal coordinate and ϕ the toroidal coordinate. It is shown in figure 2.2 along with the conventional cylindrical (R,Z,ϕ) system. In addition, the arrangement of the magnetic field lines into nested flux surfaces also allows the use of a different, and for some problems more native, set of coordinates. The flux coordinate system uses the normalized magnetic flux Ψ_N instead of r as a radial coordinate, which is easily possible, since the flux is constant on every flux surface, with strictly monotonously increasing or decreasing values from the center to the edge. Different variants of the flux coordinates exist that e.g. also assign new definitions to the poloidal coordinate.

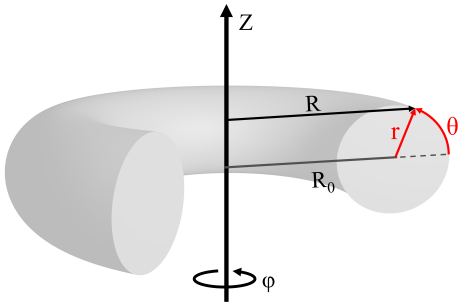

Figure 2.2: The (R,Z,ϕ) coordinate system and the (r, θ, ϕ) coordinate system. In the flux coordinate systems r is replaced by Ψ_N (own figure)

2.3 Tokamak

2.3.1 The tokamak configuration

The *tokamak* is a confinement device that generates roughly the magnetic field configuration shown in figure 2.1, which has been found as a solution to the Grad-Shafranov equation. To achieve this, tokamaks are equipped with different sets of magnetic coils, a schematic drawing is provided in figure 2.3. The toroidal and poloidal component that compose the total helical field are generated separately. The toroidal field is provided directly by the toroidal field coils. The poloidal component of the field is added by the plasma current itself, which is driven by a central solenoid that acts as a primary transformer loop. An additional small poloidal contribution that balances the hoop force comes from the poloidal field coils

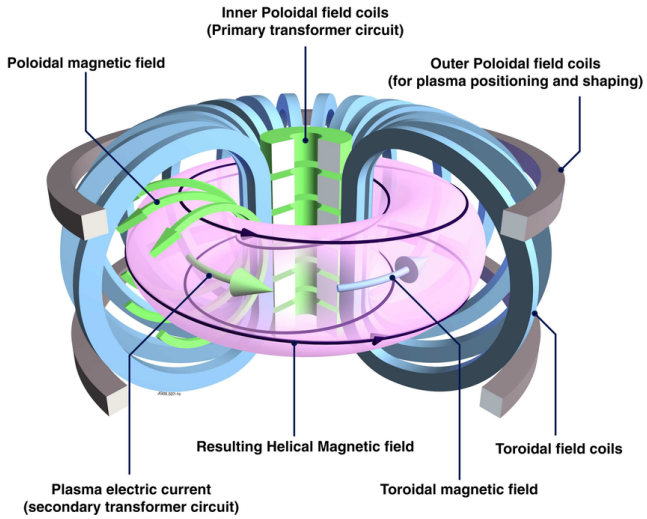

Figure 2.3: Schematic drawing of a tokamak. The helical field results from the superposition of the toroidal field from the toroidal field coils, and the field generated by the plasma current. Poloidal field coils help to balance and shape the plasma. **[JET-EFDA]**

The poloidal field coils can also be used to modify the shape of the cross section. Diverging from a simple circular cross-section, e.g. by increasing the elongation or triangularity of the plasma, can alter, and possibly improve, the performance of the plasma. With sufficiently high current in the shaping coils it is possible to create so-called *X-points*, where the poloidal field strength is zero. Figure 2.4 shows an example of a field configuration with X-Point. The flux surface that intersects the X-point is called *separatrix*. In a tokamak configuration the separatrix encloses the *closed flux surface region*, which is the toroidally confined region of the plasma. For

this reason the separatrix is also called last closed flux surface (LCFS). The field lines outside the separatrix in the *open flux surface region* intersect material components of the tokamak. Due to the high transport along the field lines these parts are subject to high heat and particle fluxes. In most modern tokamaks the open field lines are directed towards the so-called divertor, a specifically designed component that is capable of enduring these fluxes. The X-point configuration and the divertor provide a convenient way to deal with power and particle exhaust. The ASDEX Tokamak in Garching was the first tokamak to feature this component.

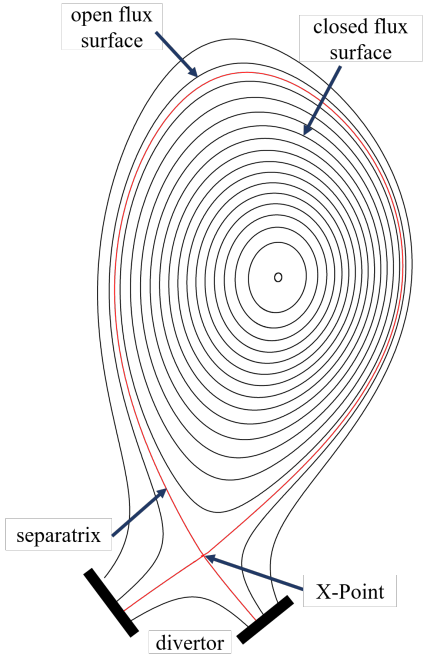

Figure 2.4: X-Point configuration. The closed flux surface region is separated from the open flux-surface region by the separatrix. The field lines in the open flux surface region, as well as the separatrix, intersect the material structures in the divertor region. (own figure)

2.3.2 H-Mode

An important milestone in the history of the tokamak was the discovery of the *H-Mode*, or high confinement mode, by Friedrich Wagner at ASDEX [18]. It is an operating regime with particularly good confinement properties that is accessed when the external heating power exceeds a certain threshold value. The transition from the low confinement mode (L-Mode) occurs abruptly. The physical mechanism

behind the transition is not yet fully understood, but it is believed that the suppression of turbulence by sheared flows plays an important role [19]. One of the main characteristics of an H-Mode plasma is the transport barrier that forms just inside the separatrix. The strongly reduced transport leads to the formation of a *pedestal* in the pressure profile (figure 2.5), which helps to improve fusion performance at equal heating power. The steep pressure gradient of the pedestal also causes a high toroidal current density at the edge. The underlying mechanism is the generation of a so-called bootstrap current, which is a current proportional to ∇p [20].

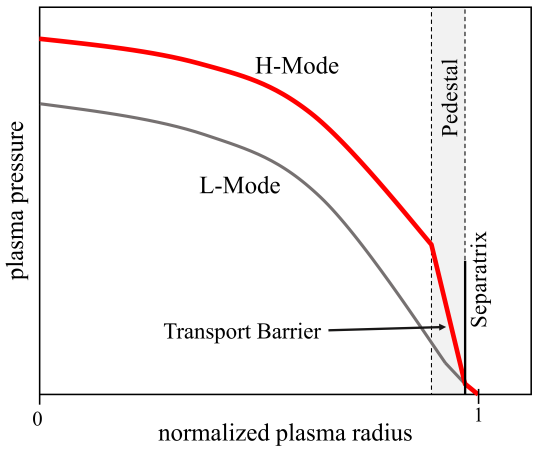

Figure 2.5: A typical H-Mode profile features a characteristic pedestal region. It is associated with a steep pressure gradient due to the transport barrier right inside the separatrix. (own figure)

2.3.3 Plasma flows in tokamaks

Another important feature of a tokamak plasma are the plasma flows that establish, especially those perpendicular to the field lines. There exist different types of flows with different sources, two of them will be discussed here briefly, namely the $\boldsymbol{E} \times \boldsymbol{B}$-flow $u^{\boldsymbol{E}\times\boldsymbol{B}}$ and diamagnetic flow u^{dia}.

$$u^{\boldsymbol{E}\times\boldsymbol{B}} = \frac{\boldsymbol{E} \times \boldsymbol{B}}{B^2} \tag{2.23}$$

$$u^{dia} = \frac{\boldsymbol{\nabla} p_s \times \boldsymbol{B}}{\rho_s B^2} \tag{2.24}$$

The diamagnetic flow is a pressure-driven flow, that has practically equal magnitude, but opposite directions, for electrons and ions. The combination of electron and ion flow results in a current perpendicular to the magnetic field lines, the *diamagnetic current* $j_{dia} = -\frac{\nabla p \times \boldsymbol{B}}{B^2}$.

In the pedestal of an H-Mode plasma, the $\boldsymbol{E} \times \boldsymbol{B}$-flow is also proportional to the pressure gradient. In this region, the E_r-profile features a well, that has been experimentally found to to be proportional to $\nabla p_i/(en_i)$ [21]. The $\boldsymbol{E} \times \boldsymbol{B}$-flow is therefore directed opposite to the ion diamagnetic flow, and in total the ion fluid is almost at rest.

2.4 Stability

2.4.1 The energy principle

The magnetic field configuration of a tokamak was found as a solution to the equilibrium condition. However, to fulfill its purpose in nuclear fusion, the plasma equilibrium also needs to be macroscopically stable. The stability of a plasma is determined by its response to a small perturbation. When a plasma in a stable configuration is perturbed, it reacts with a restoring force that damps the perturbation. In an unstable configuration the perturbation would be amplified and grow into an instability.

One of the simplest methods to examine plasma stability within the ideal MHD picture is the *energy principle*. It relies on the idea that a configuration is stable if every possible small plasma displacement $\boldsymbol{\xi}$ from the perturbation results in a positive change of potential energy of the system ($\delta W > 0$). In case of a displacement that lowers the potential energy ($\delta W < 0$) the system is unstable. To arrive at an expression for δW the MHD equations are linearized and all perturbed quantities are expressed in terms of $\boldsymbol{\xi}$. The potential energy of the system can then be expressed in terms of three contributions, that of the plasma volume δW_p, the plasma surface δW_S and the vacuum δW_V

$$\delta W = \delta W_p + \delta W_V + \delta W_S. \tag{2.25}$$

The contribution from the vacuum is generally positive and that of the surface is negligible in the absence of surface currents. The expression for $\partial W_p(\boldsymbol{\xi})$ derived from the linearized MHD equations is given by [22]

$$\begin{aligned}\delta W P = \frac{1}{2} \int_{plasma} \Bigg[& \frac{B_{1\perp}^2}{\mu_0} + \frac{B_{1\perp}^2}{\mu_0}(\nabla \cdot \boldsymbol{\xi}_{1\perp} + 2\boldsymbol{\xi}_{1\perp} \cdot \boldsymbol{\kappa})^2 + \gamma p_0 (\nabla \boldsymbol{\xi})^2 \\ & - 2(\boldsymbol{\xi}_\perp \cdot \nabla p_0)(\boldsymbol{\kappa} \cdot \boldsymbol{\xi}_\perp) - \frac{j_\parallel}{B_0}(\boldsymbol{\xi}_\perp \times \boldsymbol{B}_0) \cdot \boldsymbol{B}_1 \Bigg] dV\end{aligned} \tag{2.26}$$

Here, the subscripts $\perp$ and $\parallel$ refer to the direction perpendicular and parallel to the equilibrium magnetic field. $\boldsymbol{\kappa} = (\boldsymbol{B}_0 \cdot \nabla)\boldsymbol{B}_0/B_0$ is the curvature of the magnetic field.

The contributions of the first three terms are always positive and therefore stabilizing. The last two terms can take on either a positive or a negative sign. They have the potential to drive MHD instabilities. The second-to-last term in equation 2.26 is proportional to the pressure gradient. The contribution is destabilizing if the field line curvature is parallel to the pressure gradient, which is the case on the low-field side of a tokamak. If a mode is unstable due to the contribution of this term, the resulting instability is called *pressure-driven instability*. Similarly, the last term in equation 2.26 expresses that a current density parallel to the equilibrium field lines can destabilize the system. If this term is the dominantly destabilizing one, the instability is referred to as *current-driven instability*. However, in reality this distinction is not very strict as many MHD instabilities are a combination of both.

2.4.2 Edge-localized modes

A prominent example for an MHD instability that is both pressure- and current driven is the Edge-localized Mode (ELM). It occurs in the edge region of H-Mode plasmas, which features both a steep pressure gradient and a high parallel current density.

ELMs are characterized by rapid expulsions of heat and particles from the edge. Several percent of the pedestal energy are expelled from the plasma within fractions of a millisecond, which flattens the pressure and density gradients. In the phase following an ELM crash the degraded pedestal is rebuilt until another ELM-crash occurs. This cyclic behavior is typical for ELMs. They are often classified by the length of such a cycle (or the *repetition frequency* ν_{ELM}) with respect to the expelled power. The two main kinds are the *Type-I ELMs*, which show a lower repetition frequency and higher power output, and the *Type-III ELMs*, which are more frequent but smaller ELM crashes [23]. In the rest of this thesis type I ELMs are meant when referring to ELMs.

The physical understanding of ELMs is not yet complete, but many important aspects of their onset are explained well by the *peeling-ballooning model* [24]. The peeling-ballooning model assumes that an ELM crash is triggered by the coupling of two basic edge instabilities: a pressure driven ballooning mode and a current driven peeling mode. The linear stability limits of the two individual modes are illustrated in figure 2.6. According to this theory, the plasma parameters follow the trajectory in the stability diagram during an ELM cycle. The starting point of the cycle is a state of low pedestal current and pressure, e.g. after a previous ELM crash. Due to the H-Mode transport barrier, the pressure gradient steepens gradually (1) and the edge approaches the ballooning limit. Simultaneously the pressure gradient gives rise to a bootstrap current. The increased edge current density takes the plasma into the peeling-ballooning unstable region (2) and an ELM crash follows. The expulsion

of heat and particles causes the edge current density and pressure gradient to drop below the peeling-ballooning stability limit (3). From this point on the cycle restarts.

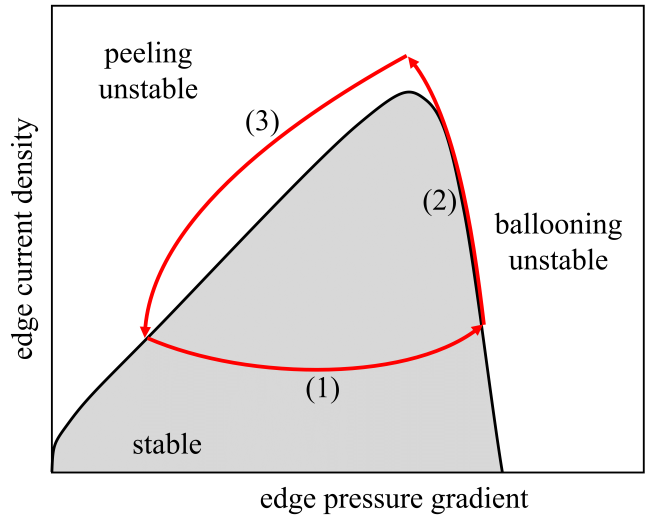

Figure 2.6: Linear stability limits of the peeling and the ballooning mode. During an ELM cycle the increasing pressure gradient (1) gives rise to a high edge current density (2), which is followed by an ELM crash (3) if the peeling-ballooning mode stability limits are exceeded. (figure recreated from [25])

Linear MHD stability analysis is sufficient to estimate the stability limits of the peeling-ballooning mode. However, it does not offer insights regarding the non-linear evolution of the mode. The linear model is not capable of making quantitative predictions about the length of an ELM cycle, the amount of energy lost during an ELM crash, or even the time-scale of the crash itself. Understanding these characteristics of the non-linear ELM phase is vital, especially for future larger tokamaks. In a tokamak of ITER dimensions scaling laws predict that the power expelled during type I ELMS could strongly reduce the lifetime of the plasma facing components [26]. The development of mechanisms to control ELMs is therefore an active field of research.

Over the past years a variety of approaches to ELM control have been studied. Some of them strive for an increase of the ELM frequency (ELM mitigation), rather than a complete elimination of ELMs (ELM suppression). This might appear counterintuitive at first, but when ELMs are triggered prematurely large ELM crashes are replaced by smaller more frequent ELMs. The result is a reduced energy flux to the plasma facing components, while at the same time the beneficial properties of ELMs are retained: The expulsion of particles during a crash removes helium ash

and impurities from the plasma. In case of complete ELM suppression, an alternative mechanism for the reduction of impurity and ash content has to be exploited.

Two main ELM control techniques are currently considered to be used in the ITER tokamak:

- **Pellet pacing**: The injection of small frozen Deuterium pellets may increase the frequency of ELMs [27] in a controlled manner. Successful ELM mitigation has been demonstrated in different tokamaks [27–29].
- **Resonant magnetic perturbations**: A set of specifically designed coils applies a small helical perturbing field to the plasma. The perturbation evokes a range of different plasma responses, which influence the confinement properties and stability of the plasma. It has been demonstrated experimentally that RMPs are capable of ELM mitigation as well as suppression.

In addition, the operation in a naturally ELM-free regime with good confinement is considered a possibility to avoid ELMs. Such regimes have been found in other tokamaks, but the extrapolation to ITER conditions is still uncertain. Alternative ELM control techniques are also under development.

Chapter 3

Resonant magnetic perturbations

Resonant magnetic perturbations are a promising method for ELM control in ITER. The first successful demonstration of RMP ELM suppression was achieved in DIII-D in 2003 [30]. Nowadays most modern tokamaks are equipped with systems suitable for RMP application, similar to the one installed in ASDEX Upgrade, which is described in section 3.1.

Subsequently either ELM suppression or mitigation has been demonstrated in numerous experiments across various devices such as ASDEX Upgrade [31], KSTAR [32], EAST [33] and JET [34]. A RMP system is also foreseen for ITER [35]. However, a reliant RMP-ELM control strategy for ITER can only be established if the underlying physical mechanisms are well understood. At the moment there are several theories that aim to explain RMP suppression or mitigation of ELMs, but not sufficient evidence to support either of them fully. RMP physics is therefore still an active field of research.

Historically, RMP penetration was treated based on the vacuum approximation model, which is presented in section 3.2. It assumes that the total magnetic field is given as the sum of the RMP field and the equilibrium field, without taking the plasma response into account. However, the disagreements between theoretical predictions and experiments made the insufficiency of this model very clear early on. The response of the plasma alters the total perturbation field significantly, and can therefore not be neglected. The implications are discussed in section 3.3. Finally, an insight into RMP-ELM control theories is given in section 3.4.

3.1 ASDEX Upgrade RMP coils

In ASDEX Upgrade the RMP system consists of a set of 16 coils placed inside the vacuum vessel at the low field side [36]. They are arranged in two rows of eight, one row above and one below the midplane, which are evenly distributed around the torus. A schematic drawing is given in figure 3.1.

The five-turn coils are each equipped with independent power supplies, which allows the adjustment of the current flow. The direction and magnitude of the coil currents are set up in a way that in total a helical perturbation field is generated. The

field is configured to have one dominant toroidal mode number, which in ASDEX Upgrade can range from $n = 1-4$. A low dominant toroidal mode number is common for RMP fields across devices. Poloidally the perturbation has contributions from a wider range of mode numbers. The poloidal mode spectrum is adjustable by shifting the toroidal phase $\Delta\Phi$ between the upper and lower coils. This is often referred to as coil phasing. As an example the $n = 2$ configuration with $\Delta\Phi = +90°$ is shown in figure 3.1b.

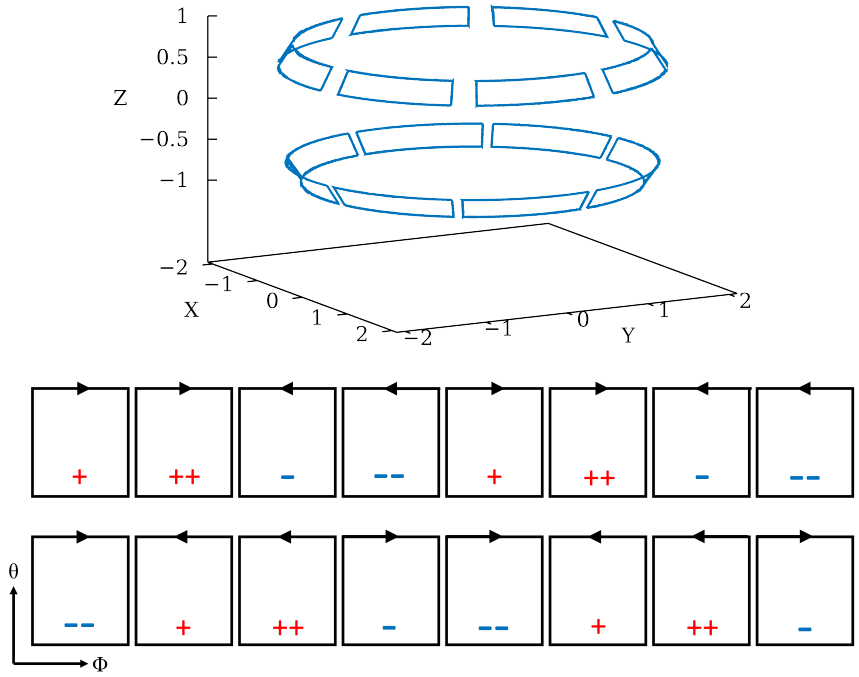

Figure 3.1: Schematic drawing of the RMP coils in ASDEX Upgrade in real space (upper part) and the (Φ, θ) plane (lower part). In the lower part the current directions of the $n = 2$, $\Delta\Phi = +90°$ configuration are indicated. The current amplitude in the coils marked with "++" and "--" is higher compared to those marked with "+" and "-", which improves the sinusoidal shape of the perturbation

3.2 Vacuum approximation

For the vacuum approximation it is assumed that the total magnetic field is given by $\boldsymbol{B}^{\mathrm{tot}} = \boldsymbol{B_0} + \boldsymbol{b}^{\mathrm{pert}}$, as a superposition of the equilibrium field $\boldsymbol{B_0}$ and the perturbation field $\boldsymbol{b}^{\mathrm{pert}}$, as it would be generated by the RMP coils in a vacuum.

The spectrum of $\boldsymbol{b}^{\mathrm{pert}}$ includes a component $\boldsymbol{b}^{\mathrm{pert}}_{m,n}$ with n, the dominant toroidal mode number of the RMP, and m, a given poloidal mode number. On the rational

surface with $q(r) = m/n$, where the equilibrium field lines complete m poloidal and n toroidal turns per revolution, the helicity of the $b^{\text{pert}}_{m,n}$ component matches the helicity of the field lines. These rational surfaces are referred to as resonant surfaces.

Resonant flux surfaces are particularly sensitive to RMPs, because $b^{\text{pert}}_{m,n}$ is constant along the field line. In each toroidal turn the plasma is subjected to the perturbation in the same direction, which displaces the field line slightly further from the equilibrium position in every revolution. Therefore even a very small perturbation leads to a considerable field line displacement.

Assuming a q-profile with $\frac{\partial q}{\partial r} > 0$, if a field line is displaced in positive r direction, it passes through a region of higher q. This causes it to advance slightly further toroidally after one full turn compared to its equilibrium trajectory. The toroidal shift continues until it moves into a region where the magnetic perturbation has the opposite sign. The process then reverses and the field line moves back towards and beyond its equilibrium position. Taking all field lines of a resonant surface together they form the structure of a so-called *magnetic island*. The *Poincaré plot* in figure 3.2 illustrates the poloidal cross section of the flux surfaces with magnetic islands. It is obtained by tracing field line trajectories and marking the position after each toroidal turn. Figure 3.3 provides a three dimensional representation of the helical structure of a magnetic island.

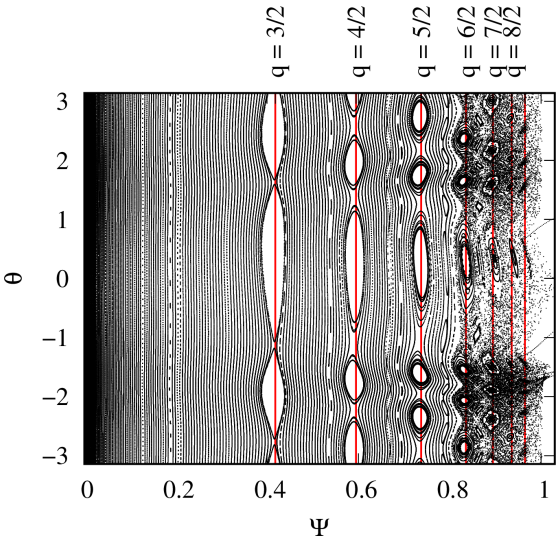

Figure 3.2: The poloidal cross section in (θ,Ψ_N) coordinates shows that magnetic islands form on q=m/n resonant surfaces when RMPs are applied. At $\Psi_N > 0.8$ the field is stochastic (own figure).

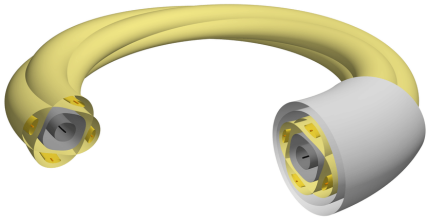

Figure 3.3: The flux surfaces of a magnetic island are nested and tube like (figure from [25])

The field lines of a magnetic island lie on nested flux surfaces which wrap around the torus in a tube-like manner. In contrast to the field lines of the equilibrium configuration, which lie on surfaces with constant Ψ_N, a field line within a magnetic island passes through different radial positions across the width of the island. As a consequence, the radial heat transport within an island is dominated by the parallel transport, which is several orders of magnitude faster than the perpendicular transport. The plasma volume enclosed by the magnetic island is thus basically lost, as it does not contribute to confinement. This is also reflected in the flattening of the pressure profile at the location of the magnetic island.

The maximum radial half-width $\delta_{m,n}$ of an island located at the $q = m/n$ flux surface can be estimated to be [37]

$$\delta_{m,n} = \left(\frac{4q^2 \left| b^{\text{pert}}_{m,n_\perp} \right|}{m(\mathrm{d}q/\mathrm{d}\Psi^{1/2})} \right)^{1/2}, \tag{3.1}$$

where $b^{\text{pert}}_{m,n_\perp}$ is the component of $b^{\text{pert}}_{m,n}$ perpendicular to the equilibrium field line. The $b^{\text{pert}}_{m,n}$ component of the perturbation, often termed pitch aligned or resonant component, impacts the island width. Above a certain threshold the islands grows so large that islands on neighboring flux surfaces begin to overlap. The degree of overlapping is given by the Chirikov parameter σ [38]

$$\sigma = \frac{\delta_{m,n} + \delta_{m+1,n}}{\Delta_{m,m+1}}, \tag{3.2}$$

where $\Delta_{m,m+1}$ is the distance between the $q = m/n$ and the $q = (m+1)/n$ rational surfaces. Chirikovs overlapping criterion predicts that overlapping islands are present if $\sigma > 1$. In these regions the local field line structure becomes increasingly complex until it is completely chaotic and no longer describable by flux surfaces. This is referred to as *ergodic* or *stochastic* field. The edge region of a tokamak plasma is particularly prone to ergodization. Here the resonant surfaces lie closer together and the associated island chains are more likely to overlap. In a region with stochastic field lines a strong radial transport is expected, as field lines undergo a radial diffusion while progressing toroidally. Due to the high electron thermal velocity electrons move along the field lines a lot faster than the heavier ions. The electron heat transport thus dominates to the stochastic transport.

The original hypothesis of RMP ELM suppression was based on this mechanism. It was thought that the increased transport would lower the edge pressure gradient below the peeling-ballooning limit, thus stabilizing the edge region. The first RMP ELM suppression experiments as well as the RMP coils planned for ITER [35] were

therefore designed to achieve a stochastic edge, quantified by the Chirikov parameter. However, similar edge stochastization turned out to have varying effects on ELMs [30, 31, 39, 40]. It became apparent that models based on the vacuum approximation were insufficient to predict ELM control and that the effects of the plasma response had to be considered.

3.3 Plasma response

The application of RMPs generates different kinds of reactions in the plasma. Some types of responses are capable of amplifying or reducing the magnitude of the perturbation compared to the vacuum approximation. The total magnetic field is then given by $\boldsymbol{B}^{\text{tot}} = \boldsymbol{B_0} + \boldsymbol{b}^{\text{pert}} + \boldsymbol{b}^{\text{plasma}}$, where $\boldsymbol{b}^{\text{plasma}}$ is the magnetic field generated by the plasma response.

3.3.1 Screening

The main effect of the screening response is the suppression of the formation of magnetic islands on the resonant surfaces. A simplified model helps to understand the basic idea, a more thorough treatment is found in [41].

In the model the plasma is reduced to a resonant surface with q(m,n), which is represented by a thin conductive layer with constant Ψ. Only the $\boldsymbol{b}^{\text{pert}}_{m,n}$ component of the perturbation field is considered. The conductive layer is rotating relative to the static perturbation with a slip frequency ω. This setup resembles that of an induction motor, and in an analogous manner, helical mirror currents are induced in the conductive layer. The mirror currents in turn induce a magnetic field $\boldsymbol{b}^{\text{plasma}}$ of the same helicity as the external perturbation $\boldsymbol{b}^{\text{pert}}$, but pointing in the opposite direction. Thus, the total perturbation is weakened compared to the vacuum approximation. In the case of an ideally conducting plasma the perturbation is canceled completely. The efficiency of the screening effect decreases with increasing resistivity.

The mirror currents have an additional effect. They exert a $\boldsymbol{j} \times \boldsymbol{B}$ torque on the resonant surface, with the direction of the torque aimed to reduce the slip velocity. The torque is counteracted by the viscous drag torque from the surrounding (non-resonant) plasma layers. The rotation slows down until a torque balance between the viscous torque and the $\boldsymbol{j} \times \boldsymbol{B}$ torque is established. If the amplitude of the external perturbation is sufficiently strong, the $\boldsymbol{j} \times \boldsymbol{B}$ torque outweighs the viscous torque. As a result, the velocity at the resonant surface is brought to zero locally. Without the differential velocity between the plasma layer and the perturbation the generation of eddy currents is stopped abruptly, and no further screening takes place. When the coil current amplitude is increased over time, this leads to a bifurcation from a state with small islands that are rotating with the plasma to a state with large, stationary islands. The transition is called locked mode onset.

The efficiency of the screening varies radially with the plasma parameters, in particular with the plasma rotation. It should be noted that from two-fluid modeling the perpendicular electron velocity $v_{e,\perp}$ arises as the relevant rotational quantity, instead of the plasma fluid velocity [42–44].

In the core of the plasma the screening effect is generally rather robust. In most cases, the rotation is strong and the resistivity is low due to the high temperatures, therefore the mirror currents are typically sufficient to completely shield the resonant component of the perturbation field. Efficient core screening is a strict necessity to be able to use RMPs for ELM control, because the substantial confinement degradation associated with island formation in the core has to be avoided. This circumstance poses an upper limit on the coil current amplitude.

At the edge the conditions are quite different. The lower temperatures and weaker plasma rotation would suggest an inefficient screening. Indeed, if mode penetration occurs, it usually takes place at the plasma edge first. However, in the pedestal region of an H-Mode plasma, the $\boldsymbol{E} \times \boldsymbol{B}$- and diamagnetic rotation provide large contributions to the velocity of the electron fluid. The additional rotation is often sufficient to screen RMP fields. There are two notable exceptions: One is the bottom of the pedestal, where high resistivity inhibits efficient screening. This region is often found in a stochastic state. The other exception is dependent on the electron velocity profile. If the electron perpendicular velocity reverses ($v_{e,\perp} = 0$) close to a resonant surface, the formation of a magnetic island is very likely. We will see in section 3.4, that this is the base for one of the ELM control theories.

3.3.2 Amplification

Apart from the screening response another type of plasma response is often observed. Resonant magnetic perturbations can couple to and drive marginally stable MHD modes [45–47]. In the cases relevant for ELM-RMP investigations the peeling mode and the ballooning mode are close to their stability limits. The high n ballooning mode does not couple easily to the low n RMPs, and therefore does not play a role for the plasma response. On the other hand, the low-n peeling mode (also called kink mode) couples easily to the RMPs. The observed amplification of modes just above the resonant modes ($m > qn$) is called kink response. It is typically separated into the *core kink response* and the *edge kink response*. The core kink response is characterized by the excitation of modes with low poloidal mode numbers, with the strongest amplification occurring in the core of the plasma. In contrast, the edge kink response causes the excitation of higher poloidal mode numbers and is restricted to the edge region. The name "kink response" refers to a characteristic kinking of the field line, which, at the edge, is related to the deformation of the plasma boundary and a displacement of the X-Point. The magnitude of the edge kink response varies

with the poloidal spectrum of the RMPs, and is therefore strongly dependent on the differential phase between the upper and lower coils.

The edge kink mode may couple to and amplify the resonant component of the perturbation [12]. It can prevent the screening of the RMPs at the edge. Since the pitch aligned component is related to the magnetic islands width, rotation braking and the deformation of the boundary, a strong edge kink amplification is thought to play an important role for ELM suppression and mitigation [12, 13, 48–50].

3.3.3 Poloidal Spectrum of the perturbation

The poloidal spectrum of the perturbation can be influenced by the coil configuration and the plasma response. It determines to a large extend the effects the RMPs have on the plasma and possible ELMs.

The poloidal mode spectrum can be illustrated particularly well with a 2D spectral analysis like the one shown in figure 3.4a. The $n = 2$ component of the perturbed flux $\Psi_{\mathrm{pert,n=2}}$ is split into the contributions from the individual poloidal harmonics m, and plotted over the normalized magnetic flux Ψ_N as radial coordinate. The radial positions where $q(\Psi_N) = m/n$ (with n=2) are marked with white crosses for each poloidal harmonic. The $\Psi_{\mathrm{pert,n=2}}$ values at these locations correspond to the pitch aligned (resonant) components of the perturbation. They can be extracted from the 2D spectral analysis and plotted as a radial profile, where the (m, n)-resonant component is given at the Ψ_N position of the (m, n)-flux surface. An example of the radial profile of the resonant component is given in figure 3.4b.

Another line is indicated with red markers in the spectral analysis. It highlights the $(m+2, n)$-component of the perturbation, which is associated to the kink modes situated just above resonance. The poloidal components with lower m corresponds to the core kink response, while the higher m modes form the edge kink response. In analogy to the radial profile of the resonant components the kink components can also be plotted as a radial profile. The $(m + 2, n)$-kink components are given at the Ψ_N position of the (m, n)-flux surface, as is shown in figure 3.4c.

3.4 ELM control with RMPs

Access to ELM suppression and mitigation with RMPs is only given for a limited region in parameter space. An important and partially still open question is to determine how and why the individual parameters like collisionality, edge density, edge safety factor, plasma shape or plasma rotation limit the access windows. Apart from the equilibrium parameters the coil configuration has to be considered as well, including the choice of amplitude of the coil current, the dominant toroidal mode number or coil phasing. For some of the parameters general or machine-specific limits have been found in experiment and modeling [31, 51–54]. However, an encompassing

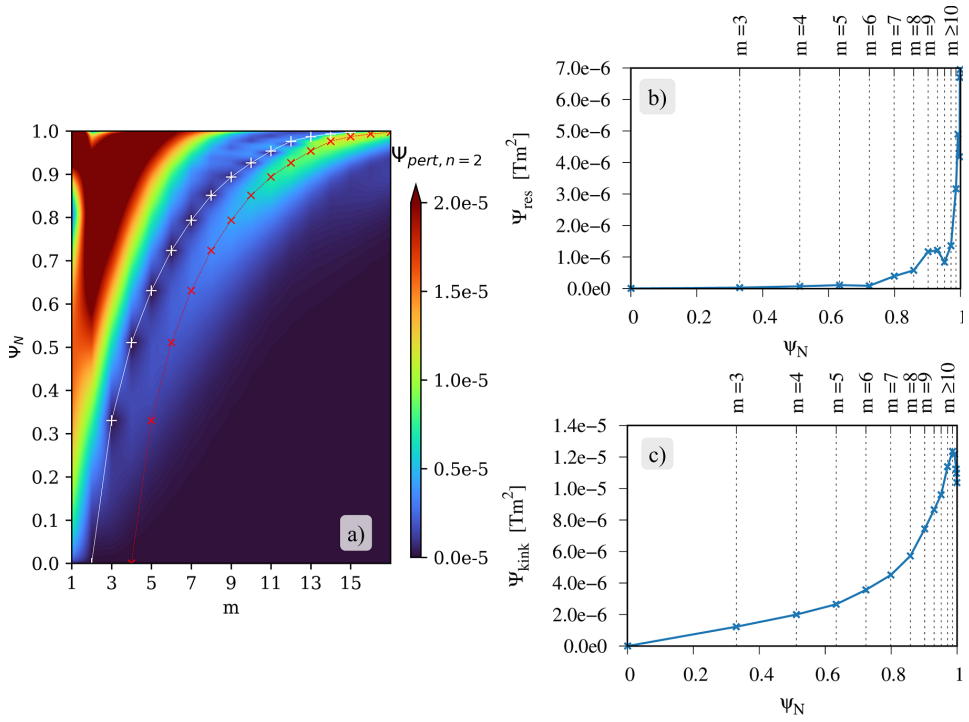

Figure 3.4: a) Exemplary 2D RMP mode spectrum including the plasma response, given over the poloidal components m and the radial coordinate Ψ_N. The (m, n)-pitch aligned component of the perturbation are marked with white crosses. Its radial profile is given in figure b. Figure c gives the (m+2,n)-kink component, which is indicated with red marks in figure a.

theory that fully explains the physical mechanisms behind ELM control and relates the access windows across devices is still lacking. There are currently several working theories based on modeling and experimentally found effects.

A phenomenon that frequently accompanies ELM suppression and mitigation is the reduction of the edge density [55, 56], commonly referred to as "density pump-out". The edge stochasticity is unlikely to provide the main contribution to the pump-out, as it primarily increases the heat transport. The expected associated drop in temperature is observed, but it is far less drastic than that of the density. The actual origin of the density pump-out is still under investigation [57]. It could be assumed that density pump-out alone is sufficient to cause ELM mitigation, by reducing the pressure gradient below the peeling ballooning mode threshold. To check this assumption cases with and without RMPs with similar pedestal parameters have been compared. In both modeling [11] and experiment [58], ELM suppression is

only found for the case with applied RMPs. While it is therefore unlikely that the pressure reduction alone is responsible for ELM mitigation, the density pump-out could still play a vital role in the overall mechanism and further non-linear effects are likely contributing [10, 13].

The formation of a large island at the pedestal top is investigated [59, 60] as another explanation for ELM control. This theory requires that the electron velocity profile features a zero crossing at the position of a resonant surface located at the top of the pedestal. Without the rotation no screening takes place and the RMPs penetrate and form locked modes. Subsequently an island forms at the top of the pedestal, strongly enhancing the local transport and flattening the pressure profile, which prevents the pedestal from growing in width. The reduced width keeps the edge region in a peeling-ballooning mode stable regime.

An alternative theory attributes ELM control to the deformation of the plasma boundary. The helical RMPs perturb the boundary sinusoidally, which leads to the formation of lobe-like structures around the X-point [61]. When the lobes intersect with the divertor, the edge transport may increase, which is expected to modify the edge profiles. In addition, stability analysis shows [62] that the boundary deformation may lower the peeling-ballooning stability limits, which could cause ELMs to be replaced with continuous transport across the transport barrier.

Chapter 4

Computational Framework

The variety of physical mechanisms discussed in the previous chapter demonstrates that the use of advanced physical and computational tools is a necessity to investigate the RMP plasma response. While ideal MHD is sufficient for basic equilibrium and stability considerations, it does not capture the complex mechanisms of the plasma response well. Instead the non-linear reduced MHD picture is used as model in this thesis . It is implemented in the highly parallelized code JOREK, which uses a finite element method and a fully implicit time stepping scheme to solve the equations in realistic X-Point geometries. Due to its modularity JOREK offers various physics models with different extensions, which provides advantages for different problems. For the scope of this thesis an extended reduced MHD version of JOREK is used together with the free boundary extension STARWALL. In the following, brief introductions to the codes JOREK and STARWALL are provided in chapter 4.1 and chapter 4.2 respectively. The chapters outline the information given in [1], where a detailed description of the design and full capabilities of JOREK can be found.

4.1 JOREK

4.1.1 Physics model

Reduced MHD is a simplified version of the full, resistive MHD model. It has the advantage of using fewer variables to describe the system, which lowers the computational cost. In addition, due to assumptions made to the velocity the fastest MHD dynamics are removed, so that larger time steps can be used in the simulation.

The derivation of the set of reduced MHD equations used in JOREK is based around the assumption that the total magnetic field is dominated by its toroidal component ($|\boldsymbol{B}_\phi| \gg |\boldsymbol{B}_{pol}|$), and that $\boldsymbol{B}_\phi$ is constant in time. This assumption allows to reformulate the magnetic field and the velocity as follows:

$$\boldsymbol{B} = F_0 \boldsymbol{\nabla}\phi + \boldsymbol{\nabla}\Psi \times \boldsymbol{\nabla}\phi \tag{4.1}$$

$$\boldsymbol{v} = R^2 \boldsymbol{\nabla}\phi \times \boldsymbol{\nabla} u + v_\parallel \boldsymbol{B} \tag{4.2}$$

Symbol	Definition
Δ^*	$R^2\boldsymbol{\nabla}\cdot(\frac{1}{R^2}\boldsymbol{\nabla})$
Δ_{pol}	$\frac{1}{R}\frac{\partial}{\partial R}(R\frac{\partial}{\partial R}+\frac{\partial^2}{\partial Z^2})$
$\boldsymbol{\nabla}_\parallel$	$\frac{\boldsymbol{B}}{\lvert B\rvert^2}\boldsymbol{B}\cdot\boldsymbol{\nabla}$
$\boldsymbol{\nabla}_\perp$	$\boldsymbol{\nabla}-\boldsymbol{\nabla}_\parallel$
$[A,B]$	$\frac{\partial A}{\partial x}\frac{\partial B}{\partial y}-\frac{\partial B}{\partial x}\frac{\partial A}{\partial y}$

Table 4.1: Definition of operators in the reduced MHD equations

where $\boldsymbol{B}_\phi = F_0/R$ and F_0 is a constant and $\boldsymbol{e}_\phi$ is the toroidal coordinate. The velocity is expressed in terms of a stream function $u = \Phi/F_0$, where Φ is the electric potential. The perpendicular velocity corresponds to the $\boldsymbol{E}\times\boldsymbol{B}$ velocity in the poloidal plane.

With these assumptions for the magnetic field and the velocity the set of reduced MHD equations can be derived from resistive MHD. They consist of five evolution equations for the five variables: the poloidal magnetic flux Ψ, the velocity stream function u, the mass density ρ, the temperature T and the parallel velocity $v_\parallel$, together with two definition equations for the current density j and the vorticity w. To simplify the notation some operators are introduced in table 4.1

The evolution equation of the poloidal flux is given by

$$\frac{\partial\Psi}{\partial t} = R[\Psi,u] - F_0\frac{\partial u}{\partial\phi} + \eta\,(j-j_0) \tag{4.3}$$

An artificial current source j_0 was defined, which can be used to e.g. keep a constant current profile over time.

The evolution of the flows is separated into two equations, the parallel momentum equation and the vorticity equation:

$$\begin{aligned}\rho B^2\frac{\partial v_\parallel}{\partial t} + \frac{1}{R^2}\rho v_\parallel\boldsymbol{\nabla}_{pol}\Psi\cdot\boldsymbol{\nabla}_{pol}\left(\frac{\partial\Psi}{\partial t}\right) =& \frac{\rho}{2R}\left[\Psi, v_\parallel^2B^2\right] - \frac{\rho F_0}{2R^2}\frac{\partial\left(v_\parallel^2B^2\right)}{\partial\phi}\\ &+\frac{1}{R}[\Psi,p] - \frac{F_0}{R^2}\frac{\partial p}{\partial\phi} + \mu_\parallel B^2\Delta v_\parallel \qquad (4.4)\\ R\boldsymbol{\nabla}\cdot\left(R^2\rho\frac{\partial\boldsymbol{\nabla}_{pol}u}{\partial t}\right) =& \left[\rho R^4w,u\right] - \frac{1}{2}\left[R^2\rho, R^2\left|\boldsymbol{\nabla}_{pol}u\right|^2\right]\\ &-\left[R^2,\rho T\right] + [\Psi,j] - \frac{F_0}{R}\frac{\partial j}{\partial\phi} + \mu R^2\Delta w\\ &\qquad (4.5)\end{aligned}$$

For the density and the temperature evolution equations the diffusion coefficients and sources have to be introduced. Here $\kappa_\perp$ and $\kappa_\parallel$ are the perpendicular and parallel

heat diffusion coefficients, $D_\perp$ is the perpendicular particle diffusion coefficient, and S_ρ and S_T are the particle and heat sources respectively. The equations are then given by

$$\begin{aligned}\frac{\partial \rho}{\partial t} =& -\rho\left(-2\frac{\partial u}{\partial Z}+\frac{1}{R}\left[v_\parallel,\Psi\right]+\frac{F_0}{R^2}\frac{\partial v_\parallel}{\partial \phi}\right)+R[\rho,u]\\ &-v_\parallel\left(\frac{1}{R}[\rho,\Psi]+\frac{F_0}{R^2}\frac{\partial \rho}{\partial \phi}\right)+\boldsymbol{\nabla}\cdot(D_\perp\boldsymbol{\nabla}_\perp\rho)+S_\rho \qquad (4.6)\\ \rho\frac{\partial T}{\partial t} =& -\rho T(\gamma-1)\left(-2\frac{\partial u}{\partial Z}+\frac{1}{R}\left[v_\parallel,\Psi\right]+\frac{F_0}{R^2}\frac{\partial v_\parallel}{\partial \phi}\right)+\rho R[T,u]\\ &-\rho v_\parallel\left(\frac{1}{R}[T,\Psi]+\frac{F_0}{R^2}\frac{\partial T}{\partial \phi}\right)+\boldsymbol{\nabla}\cdot\left(\kappa_\perp\boldsymbol{\nabla}_\perp T+\kappa_\parallel\boldsymbol{\nabla}_\parallel T\right)+S_T \qquad (4.7)\end{aligned}$$

Lastly, the current density j and the vorticity w are obtained from definition equations

$$j=\Delta^*\Psi \qquad (4.8)$$

$$w=\Delta_{pol}u \qquad (4.9)$$

JOREK solves this set of equations in their weak form. The transformation to the weak form is carried out by multiplication of the equations with suitable test functions, and integration over the whole plasma volume. Additional terms can be added to the equations to arrive at an extended reduced MHD model. This allows the inclusion of e.g. diamagnetic effects or a realistic evolution of a bootstrap current.

4.1.2 Grid construction

The weak form of the reduced MHD equations are solved on a finite element grid. JOREK uses different approaches for the spatial discretization in the toroidal and poloidal direction.

In the toroidal direction the discretization is carried out via a Fourier decomposition into $\mathrm{n_{har}}$ harmonics. The use of Fourier harmonics exploits the periodicity of the toroidal system, which lowers the computational cost. In addition, the Fourier harmonics facilitates the distinction between different physical instabilities with characteristic toroidal mode numbers.

The poloidal plane is discretized by Bezier elements. Each Bezier element is associated with a local (s,t)-coordinate system, with $0 \leq \mathrm{s} \leq 1$ and $0 \leq \mathrm{t} \leq 1$, with s,t $\perp \phi$. The physical quantities within the 2D-Bézier element are expressed in the basis of 2D-Bernstein polynomials $B^3_{i,j}(s,t)$

$$\boldsymbol{X}(s,t)=\sum_{i=0}^{3}\sum_{j=0}^{3}\boldsymbol{P}_{i,j}B^3_{i,j}(s,t). \qquad (4.10)$$

$\boldsymbol{P}_{i,j}$ denotes the physical quantity at the control point i, j of the element.

The finite element grid is set up so that the elements are aligned with the equilibrium flux surfaces, which allows for an increased numerical accuracy. Therefore, the first step in a normal JOREK simulation is the construction of the flux-aligned grid. The equilibrium flux surfaces are calculated by solving the Grad-Shavfranov equation on an initial grid. For the solution of the Grad-Shavfranov equation the pressure profile $p(\Psi_n)$ and the profile of $FF'(\Psi_n)$, with $F = RB_\phi$ and $F' = \frac{d}{d\Psi}F$ are provided as initial conditions. The pressure profile is given in terms of the temperature and density profile individually. In addition, the solver requires the poloidal flux $\Psi(R, Z)$ at the boundary as input. After an initial guess the equilibrium is found iteratively. Then, the flux-aligned grid is constructed and the equilibrium is recalculated on the new grid for better accuracy. Finally, the physical variables are initialized. An example for the initial and the flux-aligned poloidal grid is shown in figure 4.1.

4.1.3 Time stepping

Once the grid and initial values of the variables are established, the variables are evolved in time. This is done via an implicit scheme, which has the advantage that the time step size can be chosen independently of the grid size. This would not be the case for explicit schemes, which are restricted by the CFL condition [63].

For the time stepping the physical variables are summarized in the vector $\boldsymbol{u}$ and the equations are brought into the form $\frac{\partial A(\boldsymbol{u})}{\partial t} = \boldsymbol{B}(\boldsymbol{u}, t)$. The time evolution is then carried out following the scheme

$$\left[(1+\xi)\left(\frac{\partial \boldsymbol{A}}{\partial \boldsymbol{u}}\right)^n - \Delta t\theta\left(\frac{\partial \boldsymbol{B}}{\partial \boldsymbol{u}}\right)^n\right]\delta\boldsymbol{u}^n = \Delta t\boldsymbol{B}^n + \xi\left(\frac{\partial \boldsymbol{A}}{\partial \boldsymbol{u}}\right)^n \delta\boldsymbol{u}^{n-1}. \tag{4.11}$$

The change of the variables from the time step n to the time step $n+1$ is given by $\delta\boldsymbol{u}^n = \boldsymbol{u}^{n+1} - \boldsymbol{u}^n$. The parameters (θ, ξ) enable the selection of different schemes, with e.g. the $(\theta, \xi) = (1/2, 0)$ for the *Crank-Nicholson scheme*. Implicit time stepping schemes like these represent the system of equations by a large sparse matrix. The considerable computational cost of solving such a system at every time step is one of the main disadvantages of implicit schemes. However, this cost is reduced significantly in JOREK with the help of sophisticated solvers and physics-based preconditioners.

The time evolution of the quantities is usually first carried out for the axisymmetric toroidal mode ($n = 0$) only. This allows the plasma flows to establish from the initial conditions to a steady state. Once the steady state is reached, the selected non-axisymmetric ($n \neq 0$) modes are included in the simulation.

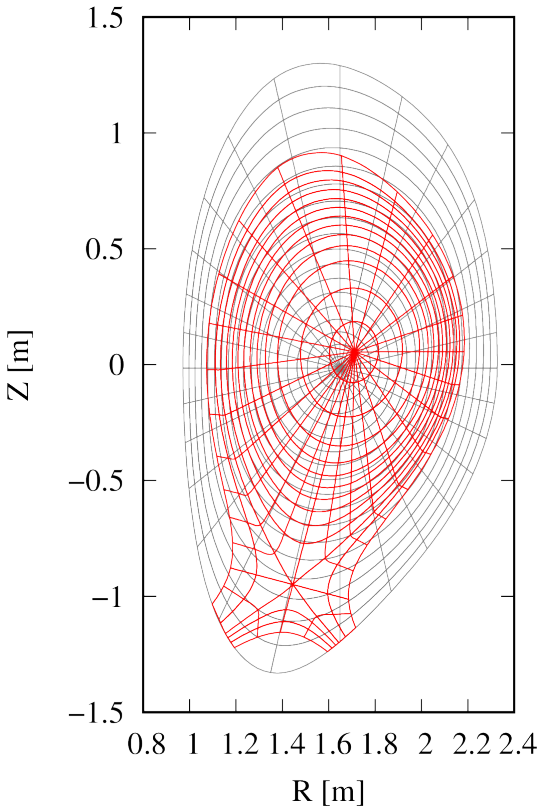

Figure 4.1: JOREK uses two types of poloidal grids: An initial grid (gray) is used to solve the equilibrium equation. Based on the equilibrium solution, a flux aligned grid (red) is constructed and used for the simulation. For clarity, the resolution of the grids is strongly reduced.

4.1.4 Boundary conditions

The modularity of JOREK can be used to employ different types of boundary conditions in the simulations. Two types of boundary conditions will be used in this thesis, termed fixed boundary and free boundary.

In *fixed boundary simulations*, Dirichlet conditions are used, so that all variables are fixed in time at the boundary. The boundary in the divertor region, where the field lines intersect the boundary, are treated separately with Bohm boundary conditions. There, the parallel velocity is set to be the ion sound speed, and free outflow conditions are set for the density. All other variables are still fixed in time at the boundary. Physically the application of Dirichlet boundary conditions to the poloidal flux and the plasma current corresponds to an ideally conducting wall at the boundary of the JOREK computational domain. In the derivation of the weak

form of the reduced MHD equations the boundary conditions appear as integrals over the boundary. With fixed boundary conditions the boundary integral in the current definition equation vanishes.

In *free boundary simulations*, the Dirichlet boundary conditions for the poloidal flux and the plasma current are removed, and natural boundary conditions are applied. As a consequence, the boundary integral in the current definition equation does not vanish anymore and has to be considered in the equations. The boundary integral can be expressed in terms of the magnetic field tangential to the computational domain boundary $\boldsymbol{B}_{\tan} = \boldsymbol{B} \times \boldsymbol{n}$, where $\boldsymbol{n}$ is the normal vector of the boundary. A suitable expression for $\boldsymbol{B}_{\tan}$ has to be found. When surrounding structures are included in the simulation, the inductances and self-inductances between different structures and the plasma have to be taken into account self-consistently and time dependently. This is the task of the STARWALL code. It provides a relation $\boldsymbol{B}_{\tan} = f(\boldsymbol{B}_n, I_C)$ between $\boldsymbol{B}_{\tan}$ and the magnetic field generated by plasma currents $\boldsymbol{B}_n$, and the imposed currents I_C in the structures. The coupling of JOREK to the code STARWALL is described in the following section.

It should be noted that the free boundary conditions can be applied to each toroidal harmonic individually. Within this thesis free boundary conditions will only be applied for the $n \neq 0$ components. This way the conducting structures do not affect the calculation of the equilibrium.

4.2 STARWALL

The STARWALL code gives the relation $\boldsymbol{B}_{\tan} = f(\boldsymbol{B}_n)$ in the form of *response matrices*. They are obtained by applying a finite element method to the set of equations, which describes the currents in the structures surrounding the plasma and the plasma currents. It consists of the Maxwells equations together with Ohm's Law for conductive structures. The problem solved by STARWALL is also called Neumann type problem. When the geometry of the plasma, walls and coils is provided, STARWALL finds a set of matrices $\underline{\mathrm{M}}_{vac}, \underline{\mathrm{M}}_{ey}$ so that the following relation is fulfilled:

$$\boldsymbol{B}_{\tan} = \underline{\mathrm{M}}_{vac}\boldsymbol{B}_n + \underline{\mathrm{M}}_{ey}\boldsymbol{Y}. \tag{4.12}$$

Here, $\boldsymbol{Y}$ is a vector containing the information of the imposed coil current I_c, as well as the induced wall current potentials Φ_{wall}. An evolution equation for the wall current potentials is also provided by STARWALL, so that the wall currents can be evolved in time by JOREK's implicit time stepping. Since the matrices $\underline{\mathrm{M}}_{vac}$ and $\underline{\mathrm{M}}_{ey}$ do not depend on the plasma dynamics, they have to be calculated only once before the start of a JOREK simulation.

For the implementation with the finite element method the conducting structures are represented by infinitely thin surfaces. The plasma volume is represented by a thin shell in which virtual surface currents flow, that generate the same magnetic field as the plasma volume. The virtual currents do not have to be calculated explicitly as they vanish naturally from the equations. With this *virtual-casing principle* the problem in STARWALL is reduced to finding the current flowing in thin surfaces separated by vacuum regions.

The thin surfaces are then discretized as triangles. Within each triangle the current is assumed constant, so that it can be approximated with current potentials at the triangle nodes.

STARWALL offers three different approaches to the implementation of coils: The first two classes of coils are either thin or broad axisymmetric bands, which are not used in this thesis. For the third class the coil is constructed from a list of points along the coil outline. This class of coils is used to create non-axisymmetric coils, such as RMP coils, in a JOREK-STARWALL simulation.

4.3 Simulation setup

In this thesis, the plasma response to RMPs in realistic ASDEX Upgrade plasmas is investigated for both fixed and free boundary simulations. The set up used for the simulations is explained in the following.

4.3.1 Equilibrium

In order to compare the effects of the boundary conditions and coil configurations the same equilibrium is used in all cases. A detailed description of the particular equilibrium configuration is found in [7], where it has been used for ELM cycle studies.

The equilibrium used in JOREK is reconstructed from a stable and stationary experimental equilibrium after an ELM-crash in an ASDEX upgrade discharge. The reconstruction is carried out by the code CLISTE [64], which extracts the equilibrium parameters from the experimental shot file. The initial temperature and density profiles are shown in figure 4.2. The edge density is relatively high, so that no RMP-ELM suppression is expected in the simulations. The q-profile is given in figure 4.3

The radial heat and particle diffusion profiles replicate an edge transport barrier, which leads to the build up of a pedestal region with steep pressure gradients at the edge. Diamagnetic effects and bootstrap currents are implemented in JOREK by the addition of extra terms. In the reduced MHD equations, the inclusion of diamagnetic effects is, among other things, necessary for the development of the E_r-well.

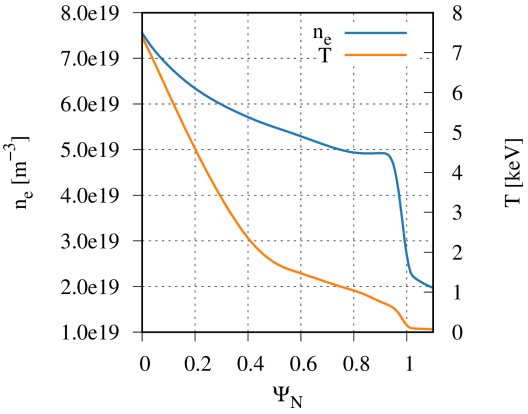

Figure 4.2: Temperature $T = T_e + T_i$ and electron density profiles n_e of the equilibrium.

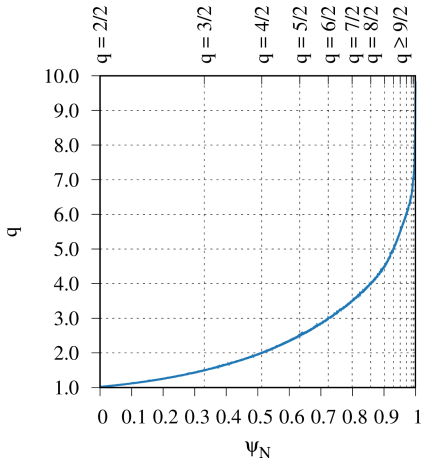

Figure 4.3: q profile of the equilibrium. The position of the q = m/2 rational surfaces is indicated by the top axis.

Only the even toroidal mode numbers between n=0 and 12 are used for the simulations. This lowers the computational cost, while at the same time retaining the important plasma dynamics.

4.3.2 Coil configuration

Several coil configurations are available with the ASDEX Upgrade set of RMP coils. In this thesis, a perturbation with dominant toroidal mode number $n = 2$ is selected. To achieve an approximately sinusoidal wave form the coil current pattern is similar to the one shown in 3.1. The effective coil current $I_C = I * n_{\text{turn}}$, where $n_{\text{turn}} = 5t$ is the number of turns in an ASDEX Upgrade RMP coil, is applied with $I_+ = 1185\,\text{At}, I_{++} = 1205\,\text{At}, I_- = -1185\,\text{At}$ and $I_{--} = -1205\,\text{At}$. For simplicity this will be referred to as $I_C = 1\,\text{kAt}$ case. For some comparisons, the coil currents are increased by a factor of 3 or 6, which will be referred to as 3 kAt and 6 kAt respectively.

4.3.3 Free boundary RMP simulations

In the simulations with free boundary resonant magnetic perturbations JOREK is used in combination with STARWALL. For the calculation of the response matrices STARWALL requires the position of the vessel wall and the coils. The wall is placed at a large distance d_{wall} to the plasma, with $R_{\text{major}} \gg d_{\text{wall}}$, so that it does not

influence the plasma dynamics. The coordinates of the 16 ASDEX Upgrade RMP coils are provided in the form of individual points.

During the simulation the RMPs are turned on shortly after the initialization of the non-axisymmetric modes, at about $t = 0.1\,\mathrm{ms}$. The coil current was ramped up to its nominal value, either $I_C = 1\,\mathrm{kAt}$ or $I_C = 3\,\mathrm{kAt}$, over 0.3 ms. The comparison between different cases are carried out once the magnetic energies have saturated.

4.3.4 Fixed boundary RMP simulations

For the fixed boundary RMP simulations the coils are not implemented directly in the simulation. Instead, the perturbation is imposed via the boundary condition of the poloidal flux Ψ. In previous JOREK fixed boundary RMP simulations the vacuum field of the RMPs at the computational domain boundary was provided by external codes, such as ERGOS [65]. For this thesis, a python script has been developed, which calculates the perturbed poloidal flux at the JOREK boundary points. The script uses the exact same list of points for the RMP geometry as STARWALL, so that differences in the plasma dynamics are not caused by inconsistencies in the coil shapes between codes.

Once the boundary conditions and discretized for the JOREK grid, they are imported at the beginning of the simulation. Again, the perturbation at the boundary is ramped up over 0.3 ms. During this phase the boundary condition for Ψ is not fixed in time. However, since the plasma dynamics are not able to influence the boundary conditions, we still refer to this as fixed boundary. Once the coil currents are fully ramped up, the boundary conditions are fixed in time.

Part II

Results

Introduction

In the following part, the results of the work carried out for this thesis are presented. First, the validation of the non-axisymmetric coils implemented in STARWALL is shown in chapter 5. The non-axisymmetric coils represent the RMP coils in the remaining simulations, so their correct functioning is essential to ensure accurate results. Chapter 6 demonstrates the first free boundary RMP simulations. A detailed analysis is carried out and the results are compared to the theoretical expectations concerning the plasma response. In chapter 7 the free boundary RMP simulations are compared to fixed boundary RMP simulations. The impact of the boundary conditions on the plasma response is investigated. Particular importance is given to the implications for the pitch aligned component of the perturbation. In addition, the influence of the completeness of the toroidal RMP spectrum is investigated, by comparing the RMP penetration when the the full spectrum is applied, compared to a reduced RMP spectrum, where only the dominant toroidal mode of the perturbation is applied. Finally, chapter 8 demonstrates the influence of the free boundary setup on ELM stability. In addition, a first demonstration of a free boundary simulation, where RMPs are applied to the ELM profile, is given. It is the first step towards ELM-RMP control simulations with JOREK-STARWALL, which will be subject to future work.

Chapter 5

Validation of non-axisymmetric coils

In the past years, numerous benchmarks have been carried out with JOREK-STARWALL [66–69]. However, the non-axisymmetric coils, which are used to represent RMP coils in the rest of this thesis, have not been covered yet by these tests. For this reason, a validation is carried out in the following.

The coils can be assumed to have been implemented accurately if the correct $\boldsymbol{B}_{\tan}$ is obtained at the JOREK boundary in a JOREK-STARWALL simulation. This quantity will therefore be used as the figure of merit. Before the results are discussed the setup is explained in section 5.1. The validation itself is split into two parts: First, in section 5.2 a basic test is carried out, which checks that in the absence of other conductors the $\boldsymbol{B}_{\tan}$ generated by current carrying non-axisymmetric coils agrees with the Biot-Savart Law

$$\mathrm{d}\boldsymbol{B}_{\tan} = \mathrm{d}\boldsymbol{B} \times \boldsymbol{n} = \frac{\mu_0}{4\pi} I \mathrm{d}\boldsymbol{l} \times \frac{\boldsymbol{r} - \boldsymbol{r'}}{|\boldsymbol{r} - \boldsymbol{r'}|^3}. \tag{5.1}$$

The second part of the validation in section 5.3 covers the interaction between surrounding passive conductive structures, such as the wall, with the coil and their joint effect on the boundary. Lastly, a correction to the STARWALL code that has been carried out in the process of this validation is discussed in section 5.4.

5.1 Validation setup

A simple circular current loop with Radius $R_C = 1\,\mathrm{m}$ is used as exemplary non-axisymmetric coil. It's center is placed at the midplane, at toroidal angle $\phi = 0°$ at 1 m distance from the computational domain boundary as shown in figure 5.1 and its current is ramped up to $I_C = 1\,\mathrm{kAt}$ at the beginning of the JOREK-STARWALL run. The plasma is removed in the simulation, so that it does not contribute to $\boldsymbol{B}_{\tan}$.

The coil is highly localized, which requires a good toroidal resolution for the tests. Therefore, the toroidal modes up to $n = 15$ are included. For the real space representation of the JOREK boundary in STARWALL $n_v = 30$ points are selected. Convergence tests have been carried out to ensure that the resolution is sufficient.

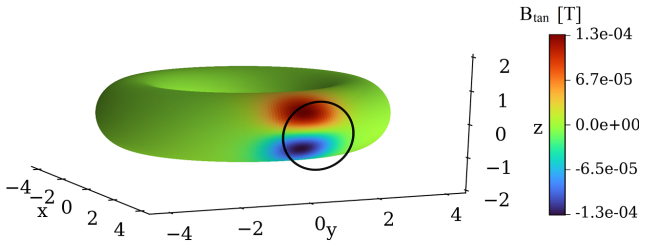

Figure 5.1: The setup for the validation of the 3D coils. The coil (black) is placed at $d = 1\,\mathrm{m}$ from the plasma boundary. The tangential magnetic field B_{tan} generated by the coil is indicated on the boundary.

5.2 Interaction of coil and plasma boundary

With the described setup the magnetic field at the computational domain boundary is calculated using JOREK-STARWALL. In the absence of a plasma and passive conductive structures the calculated field can be compared directly to the predictions of the Biot-Savart Law. Figures 5.2a and 5.2b show B_{tan} at the JOREK boundary as function of the poloidal and toroidal angle as computed by JOREK-STARWALL and a numerical implementation of the Biot-Savart Law respectively. Figure 5.2c gives the poloidally averaged absolute error as a function of the toroidal angle. The order of magnitude of the error is about two times smaller than that of the magnetic field and the shape of the magnetic field generated by the coil is practically identical between the two methods. The small remaining differences could be explained by numerical effects due to the finite resolution in the computation of B_{tan} in either JOREK-STARWALL or in the numerical implementation of the of the Biot-Savart Law.

5.3 Coil-wall interaction

The setup presented in section 5.1 is extended by a conductive wall placed between the boundary and the current loop. Two cases are investigated, one with an ideally conductive wall, and one with a highly resistive wall. In both cases, mirror currents are induced in the wall. Their magnitude and direction is shown in figure 5.3a based on the case with the ideally conductive wall. Figure 5.3b shows the time trace of the poloidally averaged absolute tangential magnetic field $|\boldsymbol{B}_{tan}|$ at the JOREK boundary close to the coil. When an ideally conductive wall is placed between the coil and the plasma, the coil magnetic field is shielded almost completely for the duration of the simulation. This implies that the magnitude and direction of the wall currents is correct, so that the induced fields cancel the external perturbation. In the case of the resistive wall similar shielding effects are observed at first. As the

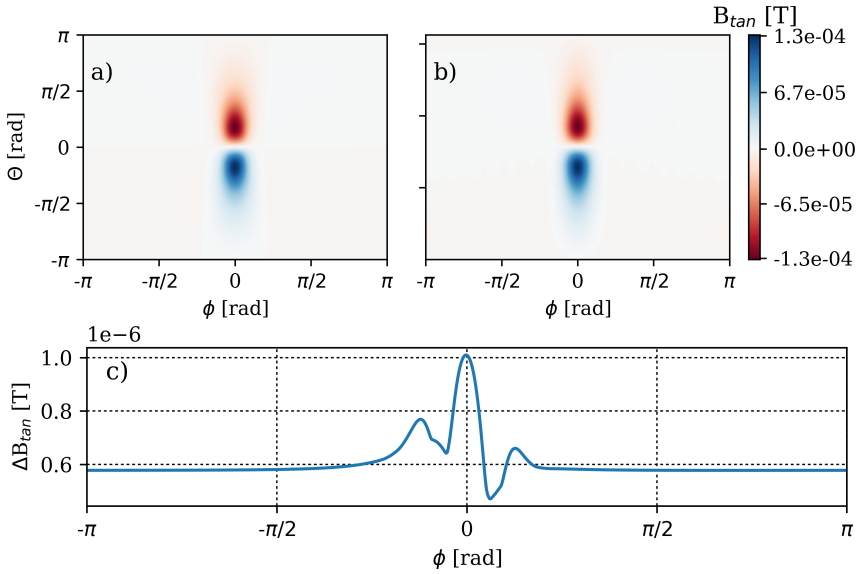

Figure 5.2: The tangential magnetic field $\mathrm{B_{tan}}$ as a function of toroidal angle ϕ and poloidal angle θ as obtained by (a) JOREK-STARWALL and (b) the Biot-Savart Law. The poloidally averaged absolute error is shown in (c).

wall currents begin to decay the influence of the wall decreases until the fields match the case without wall.

5.4 Correction to STARWALL code

In the course of this validation a correction to the STARWALL code has been carried out.

As introduced in section 4.2, $\boldsymbol{B}_{\mathrm{tan}}$ is provided by STARWALL in the form of response matrices. For the purpose here, equation 4.12 is expanded slightly, by splitting $\underline{\mathrm{M}}_{ey}$ into the individual contributions from the coils $(\widetilde{\underline{\mathrm{M}}}_{\|c}, I_c)$ and the wall $(\widetilde{\underline{\mathrm{M}}}_{\|w}, \Phi_w)$

$$\boldsymbol{B}_{tan}^{n=0} = \underline{\mathrm{M}}_{vac} B_n + \widetilde{\underline{\mathrm{M}}}_{\|w} \Phi_w + \widetilde{\underline{\mathrm{M}}}_{\|c} I_c \tag{5.2}$$

The calculation of the coefficients of these matrices requires a summation over the triangles, that represent the discretized thin surfaces of coils, walls and plasma. In addition, to match with the Fourier representation of JOREK, the matrices are calculated separately for each toroidal mode n, so that $\boldsymbol{B}_{\mathrm{tan}} = \boldsymbol{B}_{\mathrm{tan}}^{n=0} + \boldsymbol{B}_{\mathrm{tan}}^{n\neq 0}$.

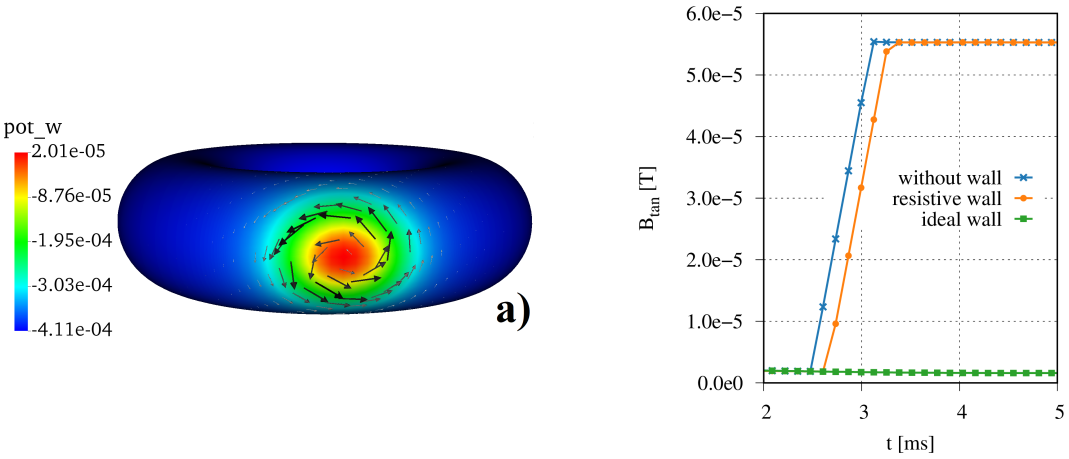

Figure 5.3: a) Induced wall current stream function pot_w and wall currents (vectors) in the ideal wall case. b) Time trace of the poloidally averaged absolute tangential magnetic field $|\boldsymbol{B}_{\tan}|$ at the JOREK boundary.

In the calculation of the axisymmetric component of the matrices an erroneous sign had been introduced in the summation over the triangles in the $\underline{\widetilde{\mathrm{M}}}_{\|w}^{n=0}$ and $\underline{\widetilde{\mathrm{M}}}_{\|e}^{n=0}$ matrices. It effectively resulted in a sign change in the matrix coefficients. Therefore the calculation of $\boldsymbol{B}_{\tan}$ was implemented as

$$\boldsymbol{B}_{tan}^{n=0} = \underline{\mathrm{M}}_{vac}^{n=0} B_n^{n=0} + (-\underline{\widetilde{\mathrm{M}}}_{\|w}^{n=0})(-\Phi_w^{n=0}) + (-\underline{\widetilde{\mathrm{M}}}_{\|c}^{n=0})(-I_c^{n=0}), \tag{5.3}$$

$$\boldsymbol{B}_{tan}^{n\neq 0} = \underline{\mathrm{M}}_{vac}^{n\neq 0} B_n^{n\neq 0} + \underline{\widetilde{\mathrm{M}}}_{\|w}^{n\neq 0} \Phi_w^{n\neq 0} + \underline{\widetilde{\mathrm{M}}}_{\|c}^{n\neq 0} (-I_c^{n\neq 0}). \tag{5.4}$$

The consequences can be considered term by term:

The first term remained unaffected.

The second term contains the effects of the induced wall potentials. The axisymmetric wall currents were induced in the opposite direction to what is foreseen, due to the sign error in $\underline{\widetilde{\mathrm{M}}}_{\|w}^{n=0}$. However, because of the cancellation of the signs the correct contribution to $\boldsymbol{B}_{\tan}$ was calculated. In comparison to the non-axisymmetric component the wall currents were induced in the opposite direction. This is physically inconsistent, but since the wall currents are linear, it does not have an impact on $B_{\tan}$. The wall currents themselves are not used for data analysis in JOREK-STARWALL.

The last term on the right hand side describes the influence of coils with externally applied currents. As a response to the incorrect sign of $\underline{\widetilde{\mathrm{M}}}_{\|c}^{n=0}$ the convention of the direction of the coil current had been changed from I_C to $-I_C$. This way, $\boldsymbol{B}_{\tan}$ was

obtained correctly for axisymmetric coils, where $\underline{\widetilde{M}}_{\|c}^{n\neq 0} = 0$. All simulations that had been carried out to this date included only axisymmetric coils. Therefore, the correct boundary conditions had been obtained for all these cases.

In the presence of non-axisymmetric coils the last term in equation 5.3 does not vanish anymore. Since the coil currents are prescribed for all modes collectively, the change of the convention of I_C combined with the correct response matrices would lead to an incorrect result. However, non-axisymmetric coils with a prescribed current are used for the first time for this validation.

To summarize, the inconsistency in the sign of the mentioned STARWALL matrices did not affect the plasma dynamics of any of the JOREK-STARWALL simulations carried out to this date. The boundary conditions were calculated correctly in all these simulations. Once the inconsistency was detected, it was resolved by adjusting the signs of the concerned matrices. Now even in the presence of non-axisymmetric coils the correct results can be obtained. The STARWALL extension is now functioning properly for both axisymmetric and non-axisymmetric coils.

Chapter 6

Free boundary RMP Simulations

In this chapter the results of the first JOREK-STARWALL RMP simulations are presented. First, in section 6.1 the results are examined and compared to the theoretical expectations, that were introduced in chapter 3. Then, the influence of the poloidal spectrum will be investigated by comparing RMP simulations with varying coil phases. Unless specified otherwise, the simulations are set up as explained in section 4.3.

6.1 General features of the plasma response to RMPs

At the beginning of the JOREK simulation the RMPs are turned off to allow the equilibrium flows to establish. Then, the current in the RMP coils is ramped up over $\Delta t \approx 0.3\,\mathrm{ms}$ to the nominal I_C value. The time evolution of the normalized magnetic energy $E_{mag,n}$ of each toroidal mode n is shown in figure 6.1a. The penetration of RMPs causes the magnetic energies to grow until a saturated state is reached. Different toroidal modes saturate at different magnetic energies, with the more dominant modes of the perturbation saturating at higher values. Here, the n=2 mode, which is the dominant toroidal mode of the perturbation, saturates at the highest value, followed by the n=6 mode, which is the strongest side band mode.

A poloidal cross section of the perturbed magnetic flux that establishes in the saturated state (at $t = 0.6\,\mathrm{ms}$) as response to the RMPs is shown in figure 6.1b. The comparison to the vacuum approximation of the flux shown in figure 6.1c gives a first impression of the impact of the plasma response, which is analyzed in detail in the following.

First, we want to focus on the effects that occur in the plasma as response to the RMPs. For this purpose three simulations with different coil currents are carried out with $I_C = 0\,\mathrm{kAt}$ (no RMPs), $I_C = 1\,\mathrm{kAt}$ and $I_C = 3\,\mathrm{kAt}$. The coil configuration $\Delta\Phi = 90°$ is selected for this comparison, but the general features discussed in this section appear for all coil configurations.

When RMPs are applied mirror currents establish in the vicinity of the resonant flux surfaces. The poloidal cross section of the $n = 2$ currents in figure 6.2a reveals

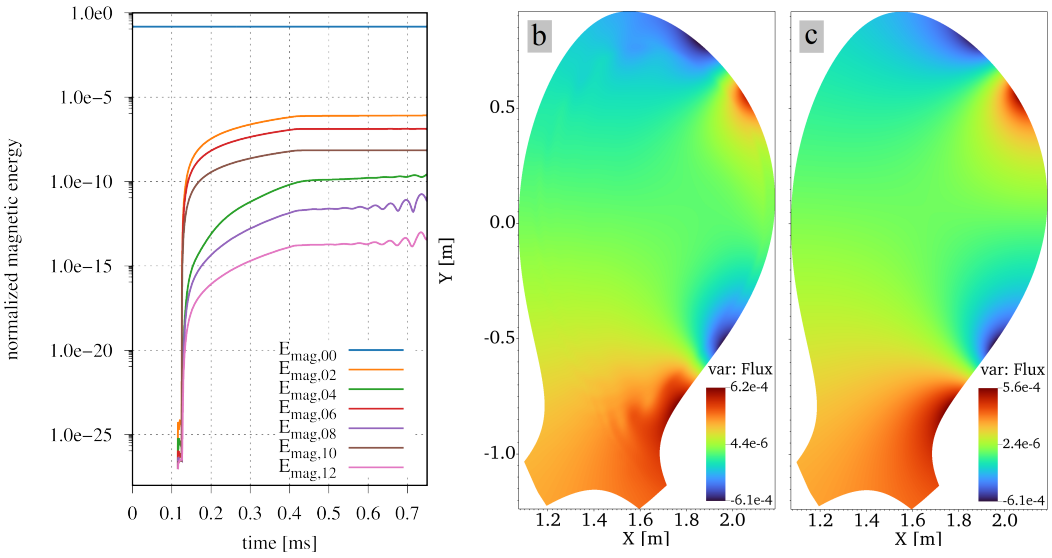

Figure 6.1: a) Time evolution of the magnetic energies of the individual modes. b) Poloidal cross-section of the total $\Psi_{n=2}$ perturbed flux including the plasma response. c) Poloidal cross-section of the total $\Psi_{n=2}$ perturbed flux in the vacuum approximation.

the helical structure of the currents. One of the effects of the mirror currents on the plasma is the reduction of the perpendicular electron velocity $v_{\perp,e}$, due to the $\boldsymbol{j} \times \boldsymbol{B}$-torque. As can be seen in figure 6.2c, $v_{\perp,e}$ is reduced when RMPs are applied ($I_C = 1\,\mathrm{kAt}$ and $I_C = 3\,\mathrm{kAt}$). The velocity braking mainly occurs close to the edge, where the largest mirror currents are induced by the RMPs. It is small for the lower coil current, but has a distinct effect at the higher coil current of $I_C = 3\,\mathrm{kAt}$. When the coil current is increased even further, mode penetration at the rational surfaces would be expected, where the electron perpendicular rotation drops to zero and the resonant perturbation including the plasma response becomes similar to the vacuum value again. However, as discussed in more detail in the following chapter, already at coil currents below the mode penetration threshold a confinement degradation is observed for this particular equilibrium. Mode penetration is therefore not shown here.

In addition to the induction of mirror currents the formation of magnetic islands chains is observed especially in the edge region of the plasma. The width of the islands increases with the coil current, which can be seen when contrasting the (Ψ_N, θ)-Poincaré plots for the three coil current amplitudes (figure 6.3a-c). It also shows that the width of the stochastic layer and the kinking of the field lines increase with I_C.

In figure 6.3d-f the Poincaré plot is shown in (R,Z)-space. Due to the distorted

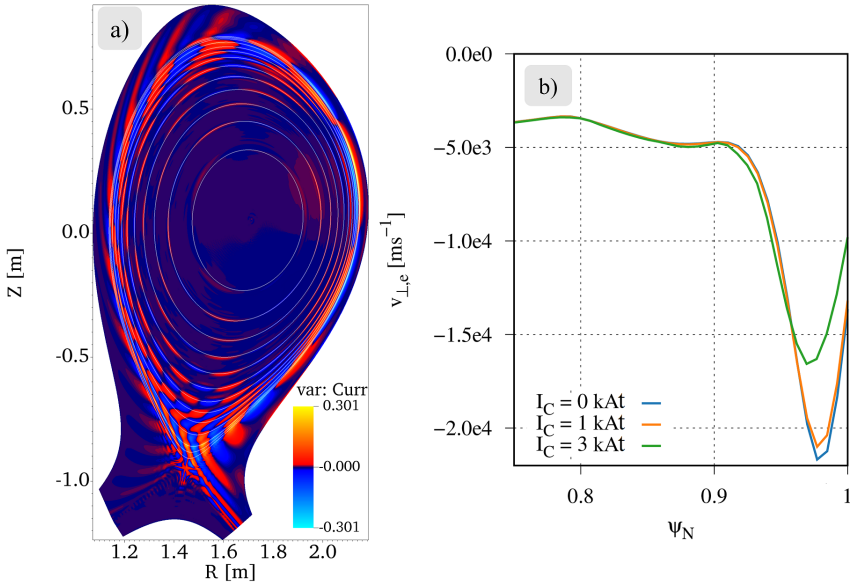

Figure 6.2: a) Poloidal cross section of the n=2 contribution of the current, showing the helical structure of the mirror currents. The (m, n)-resonant surfaces with $n = 2$ and $m = 2-14$ are marked with white lines. c) The radial profile of the perpendicular electron velocity $v_{\perp,e}$ shows the velocity braking due to the RMPs in the edge region.

boundary lobe structures form in the X-Point region. Again, the higher coil current has a greater impact and leads to the formation of longer lobes, which may contribute to a larger change in the edge transport behavior.

The plasma response described above changes the total perturbed field significantly from the vacuum approximation. The poloidal spectrum of the RMPs with and without plasma response is illustrated in the 2D spectral plot in figure 6.4. The n=2 component of the flux is shown as function of its poloidal Fourier components m and the radial Ψ_N coordinate. The radial location of the resonant flux surfaces (with $m = qn$) is indicated in the figure with white crosses.

In the vacuum approximation the RMPs clearly excite the n=2 component of the flux even around the resonant surfaces. Once the plasma response is included, the amplitude of the perturbation reduces at the location of the resonant surfaces. Especially in the core region the perturbation drops to zero, while a finite component remains at the edge. In addition to the screening response the amplification of the edge kink and core kink modes, with $m > qn$ is seen.

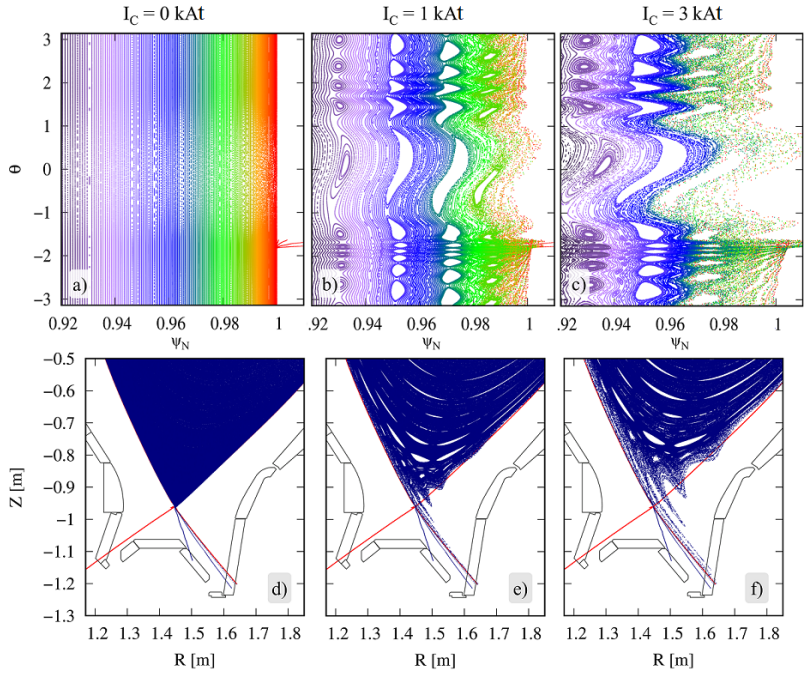

Figure 6.3: Poincare plots for different coil currents I_c in (Ψ_N, θ) space (a-c) as well as real space (d-f). Field lines that originate from the same radial position in the plasma are drawn with the same color in a-c. In d-f the position of the last closed equilibrium flux surface is marked in red and the divertor structure in black.

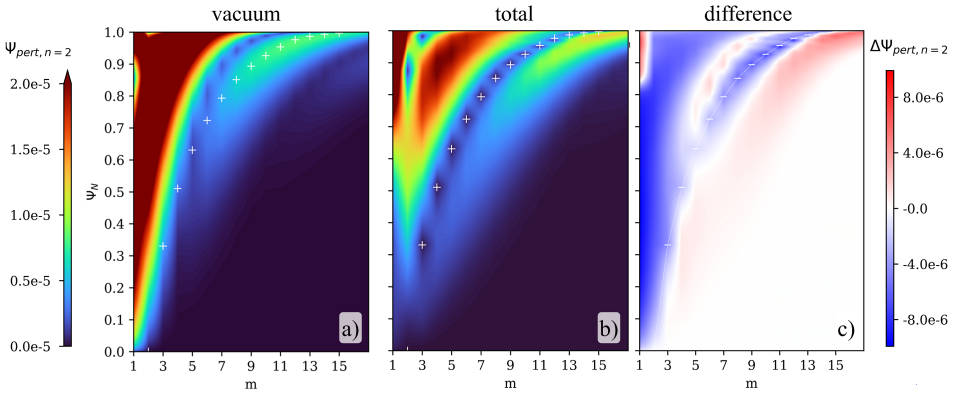

Figure 6.4: Poloidal spectrum of the n=2 flux perturbation. The magnitude of the m-th poloidal mode of the $\Psi_{n=2}$ perturbation is given over the radial coordinate for a) the vacuum case and b) the total perturbation, including the plasma response. In c) the impact of the plasma response is demonstrated by plotting the difference $\Delta\Psi_{\text{pert,n=2}} = \Psi_{\text{pert,n=2, total}} - \Psi_{\text{pert,n=2, vacuum}}$.

A note on the choice of coil current magnitude Coil currents of up to $I_C = 3\,\mathrm{kAt}$ are on the small side of what is used in ASDEX Upgrade RMP experiments. They are more typically found to be about $I_C \gtrsim 5\,\mathrm{kAt}$.

This motivated the execution of a test case with $I_C = 6\,\mathrm{kAt}$. However, the resulting conclusion is that these higher coil currents are not ideal for the studies in this thesis. They cause a strongly increased heat and particle transport, which hinders the formation of steep pressure gradients. The edge density, pressure and temperature profiles, as well as the particle and heat content, are shown in figures 6.5 and 6.6 respectively. Since the goal of this thesis is to provide a first step towards RMP-ELM control studies, the cases with a steepening pressure gradient are of greater interest. Therefore, the majority of the simulations in the remaining thesis are carried out for $I_C \leq 3\,\mathrm{kAt}$. In future studies the equilibrium may be modified, so that the plasma parameters resemble those of experimental RMP studies more closely. This should allow for higher coil currents without confinement degradation.

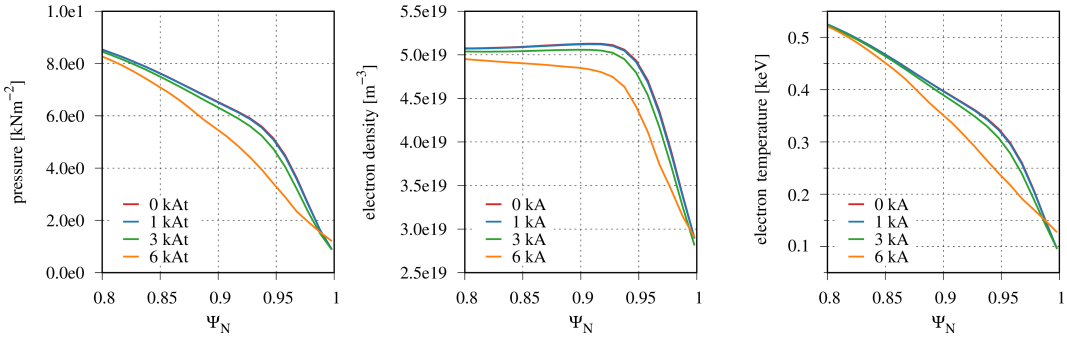

Figure 6.5: Pressure, density and temperature profiles with coil currents $I_C = 0\,\mathrm{kAt}, 1\,\mathrm{kAt}, 3\,\mathrm{kAt}$ and $6\,\mathrm{kAt}$ at $t = 0.8\,\mathrm{ms}$.

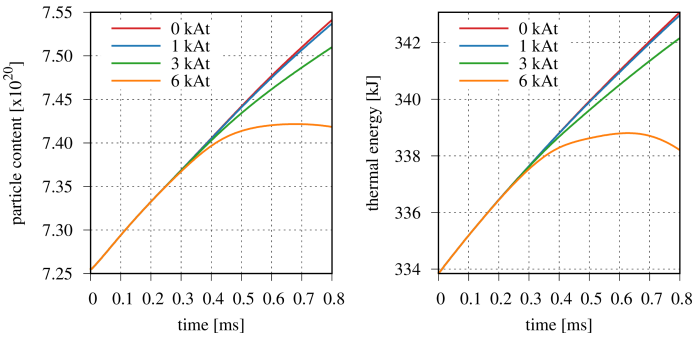

Figure 6.6: Time evolution of the particle content and thermal energy of the plasma at different RMP coil currents in the RMP penetration phase.

6.2 Impact of the coil phase on the plasma response

While the effects described in the previous section generally occur for all coil phases, their magnitude may vary. Therefore, the plasma response is examined for three different coil phases $\Delta\Phi = -90°, 0°, 90°$ for $I_c = 1\,\mathrm{kAt}$ in the following.

The spectral analysis of the n=2 component of the magnetic flux is shown in figure 6.7 for the three coil phases, together with their vacuum RMP fields, so that the impact of the plasma response can be distinguished from the mode spectrum of the coil configuration.

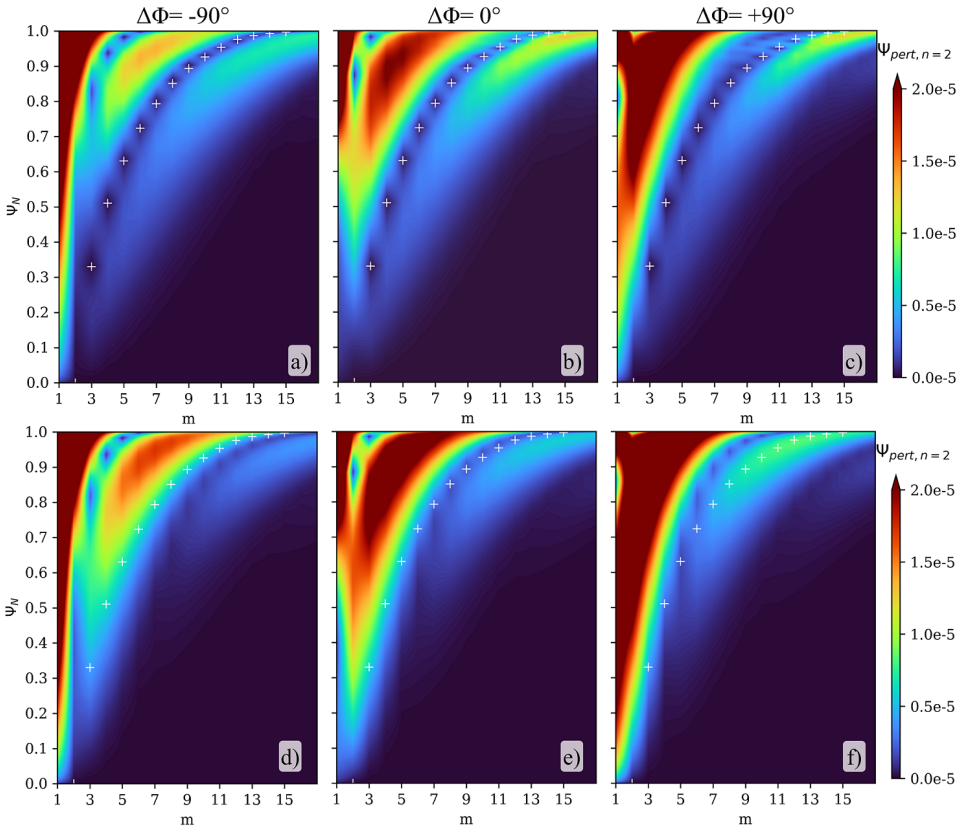

Figure 6.7: Spectral analysis of the n=2 component of the flux perturbation for free boundary RMP simulations (top) and the vacuum RMP field (bottom). Three different coil configurations with $I_c = 1\,\mathrm{kAt}$ are compared, with a coil phasing of a,d) $\Delta\Phi = -90°$, b,e) 0° and c,f) 90°

First of all, the screening of the perturbation on the rational flux surfaces is clearly observed in the core of the plasma. Especially in the core region the perturbation at the resonant surfaces is close to zero. Then, the excitation of the kink modes is seen

for all three coil cases in the free boundary simulation. It is of a similar magnitude for the $\Delta\Phi = 0°$ and $\Delta\Phi = +90°$ coil phases and weaker in comparison weak for the $\Delta\Phi = -90°$ case.

Particularly interesting is the effect of the plasma response on the resonant component of the perturbation. The resonant component influences the width of the magnetic islands and stochastic layers, length of lobes or deformation of the boundary, which are quantities that have been identified to correlate with RMP-ELM suppression. The radial profile is shown in figure 6.8. The largest pitch aligned component at the edge is obtained for $\Delta\Phi = +90°$ in both the vacuum and the total perturbation. Due to screening effects the resonant component is lowered when the plasma response is considered. With the $\Delta\Phi = 0°$ coil phasing, the excitation of the edge kink modes and their coupling to the resonant modes is large enough, so that the resonant modes are amplified above the vacuum approximation at the boundary. For the $\Delta\Phi = -90°$ the screening response is dominant and even at the plasma edge the amplitude of the perturbation is very small compared to the vacuum approximation.

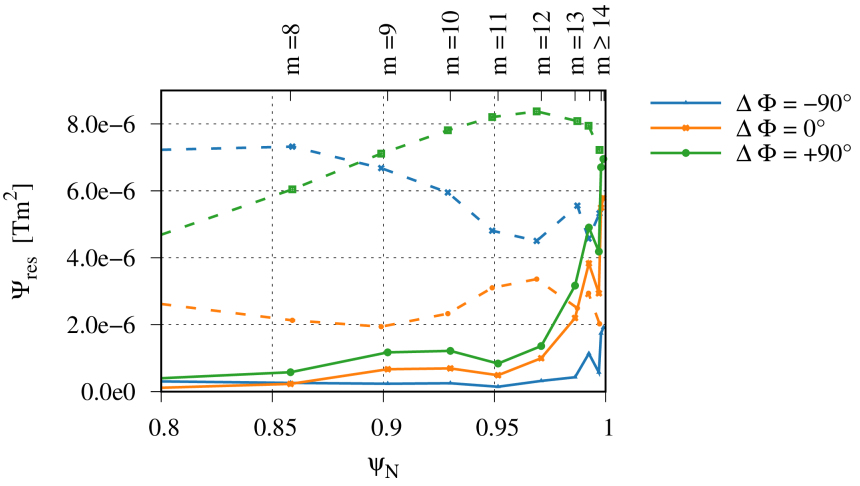

Figure 6.8: Radial profile of the pitch aligned component Ψ_{res} for the three different coil phases $\Delta\Phi$ including the plasma response (solid lines) and in the vacuum approximation (dashed lines).

The correlation of the pitch aligned component to the effects of the RMPs on the plasma is also observed in the simulations. The comparison of (Ψ_N, θ)-Poincaré plots in figure 6.9a-c shows, that, as expected, the width of the magnetic islands and the stochastic edge region is much smaller for the $\Delta\Phi = -90°$ than $\Delta\Phi = 0°$ and $\Delta\Phi = +90°$. It is also reflected in the displacement of the plasma in the X-Point

region, shown in figure 6.9d-f. Here, the deformation of the field lines around the X-Point is represented by the perturbation of the mass density ρ.

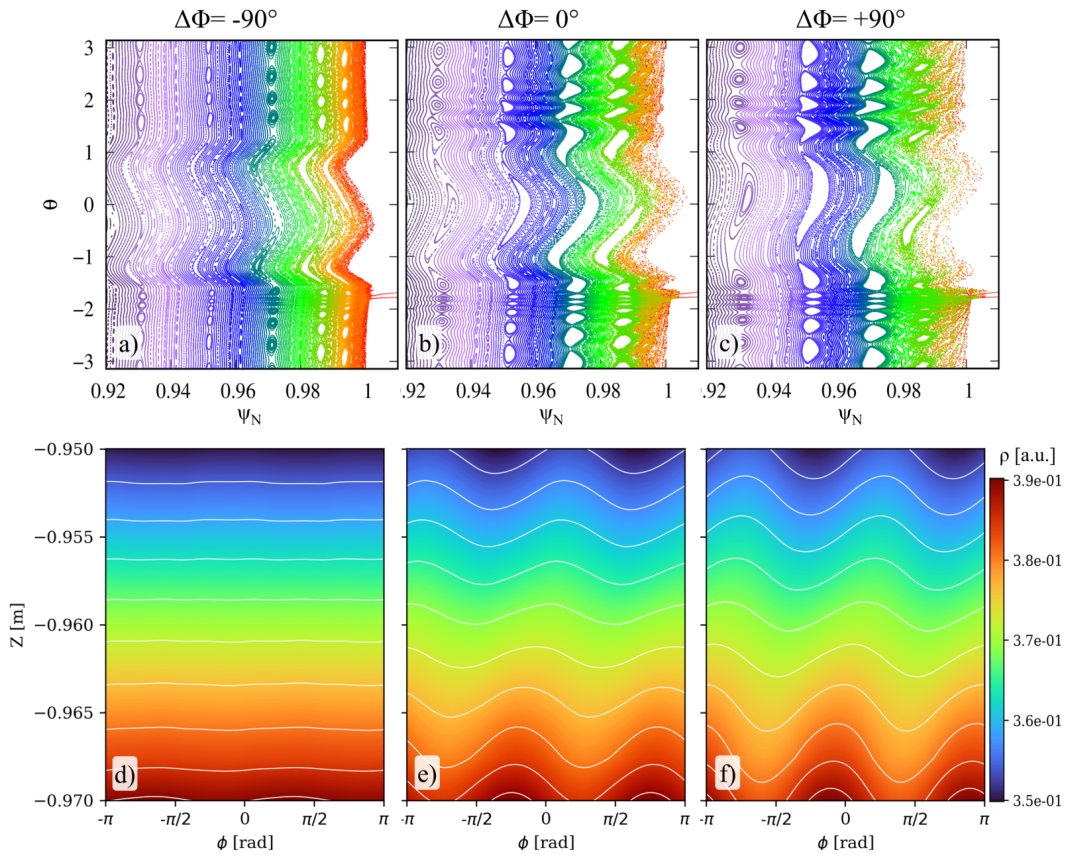

Figure 6.9: The configurations with the strongest edge kink amplification also show the largest effects on the plasma. The size of the magnetic islands and the stochastic layer (a) and the displacement of the plasma around the X-point (b) is smallest for $\Delta\Phi = -90°$, followed by $\Delta\Phi = 0°$ and $\Delta\Phi = +90°$. Some surfaces of constant density are indicated by white line, to illustrate the magnitude of the displacement.

6.3 Reduced RMP spectrum

Experimentally, RMPs are applied with a single dominant toroidal mode. However, due to the geometry of realistic coil sets, smaller sideband modes are inevitably generated. The influence of these modes can be tested by comparing simulations where

the full perturbation spectrum is applied to simulations where only the dominant toroidal mode number is applied.

In JOREK-STARWALL, the application of the reduced spectrum is achieved by using free boundary conditions only for the $n = 2$ mode. The other modes are included in the simulation with fixed boundary conditions. The comparison is carried out for the resonant case with $\Delta\Phi = 90°$ and here the coil current is increased to $I_C = 6\,\mathrm{kAt}$, so that the differences between the full and reduced RMP spectrum are more distinguishable.

The toroidal mode spectrum of the vacuum perturbation at $\Phi = 0°$ is plotted in figure 6.10. The spectrum is dominated by the $n = 2$ mode, with contributions from the $n = 6$ and $n = 10$ modes.

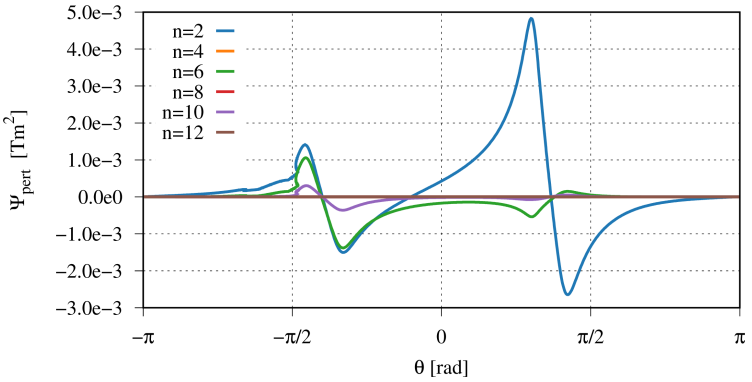

Figure 6.10: The toroidal spectrum of the applied vacuum perturbation has sidebands of $n = 6$ and $n = 10$.

The influence of the side band modes is seen clearly in the time evolution of the magnetic energies. When the full spectrum is applied (figure 6.11a), the $n = 6$ and $n = 10$ modes saturate at higher values, compared to the case where only the $n = 2$ perturbation is applied (figure 6.11b). The growth rates also indicate, that the excitation in the reduced case occurs due to coupling to the $n = 2$ mode, rather than as a direct response to RMPs.

With the sideband modes not included in the simulation, fewer magnetic island chains form, which is seen when comparing the Poincaré plots for the full and reduced RMP spectrum in figures 6.12a and 6.12b respectively. Since the distance between island chains is larger, the width of the stochastic layer is slightly smaller in the reduced case.

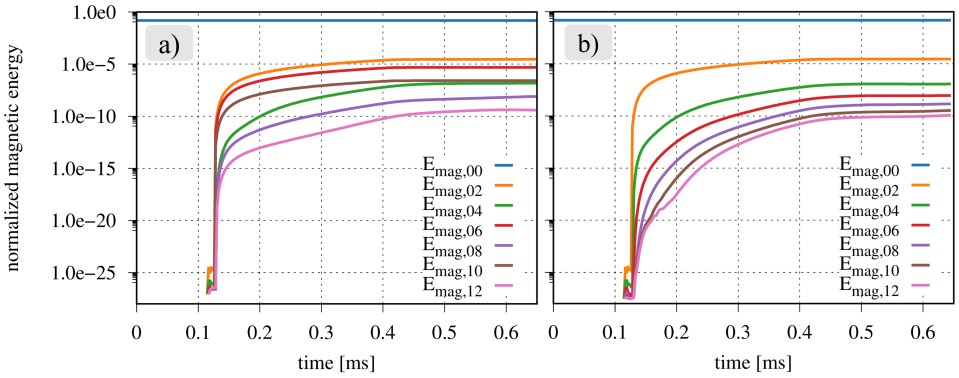

Figure 6.11: Time evolution of the magnetic energies when (a) the full perturbation and (b) the reduced perturbation spectrum is applied.

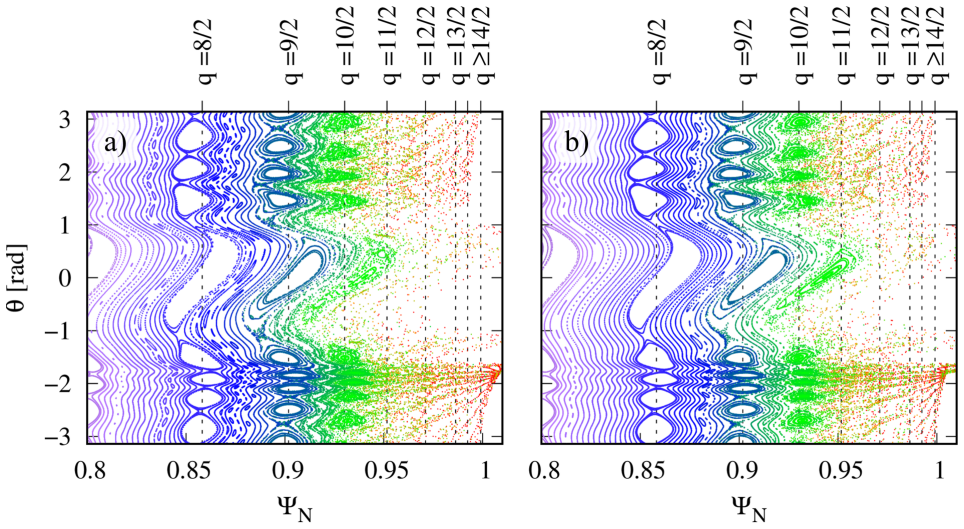

Figure 6.12: Poincaré plots of the case for the (a) full RMP spectrum and (b) reduced RMP spectrum. In (a) the sideband modes contribute to the formation of more magnetic island chains, which leads to a wider stochastic edge layer. The top axis indicates the location of the $q = m/n$ resonant surfaces of the $n = 2$ mode. Those of the $n = 6$ and $n = 10$ sidebands are not marked.

Chapter 7

Comparison of free and fixed boundary RMP simulations

Before this thesis, JOREK RMP simulations had only been carried out with fixed boundary conditions as they have been defined in section 4.1. With fixed boundary conditions, Ψ has to fulfill the vacuum approximation at the boundary, while the bulk plasma responds to the perturbation. This changes, when free boundary conditions are applied and the magnetic field can evolve freely everywhere, including the boundary. In this chapter, the RMP penetration simulated with free boundary conditions with JOREK-STARWALL, is compared to the RMP penetration calculated with fixed boundary.

The fixed and free boundary simulations are set up as described in chapter 4.3 with a coil current of $I_C = 1\,\mathrm{kAt}$. The boundary conditions are either given by JOREK-STARWALL in the free boundary case, or provided externally from numerical calculations in the fixed boundary case. Figure 7.1 shows the perturbed magnetic flux at the boundary of the computational domain in the saturated state. In the free boundary simulation, the perturbation clearly deviates from the vacuum approximation prescribed for the fixed boundary.

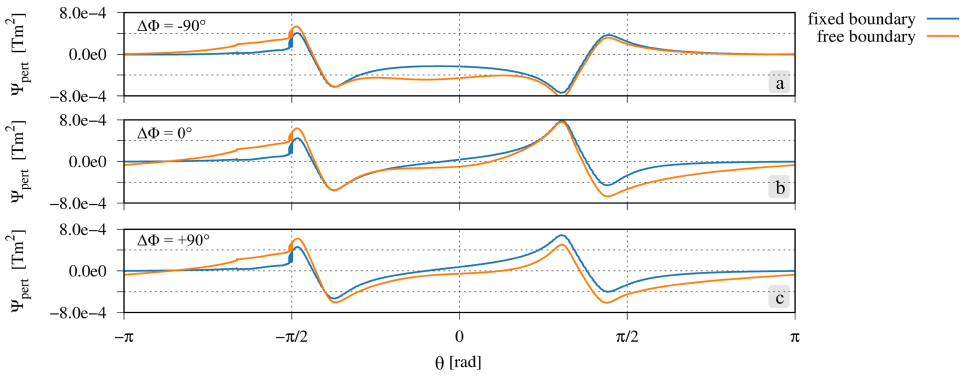

Figure 7.1: The perturbed magnetic flux at the boundary of the computational domain over the poloidal angle θ.

The different boundary conditions also affect the overall mode spectrum of the perturbation. It is illustrated in figure 7.2 for three different coil phases $\Delta\Phi = -90°, 0°, +90°$, together with the difference $\Delta\Psi$ between the free boundary and the fixed boundary perturbation spectrum.

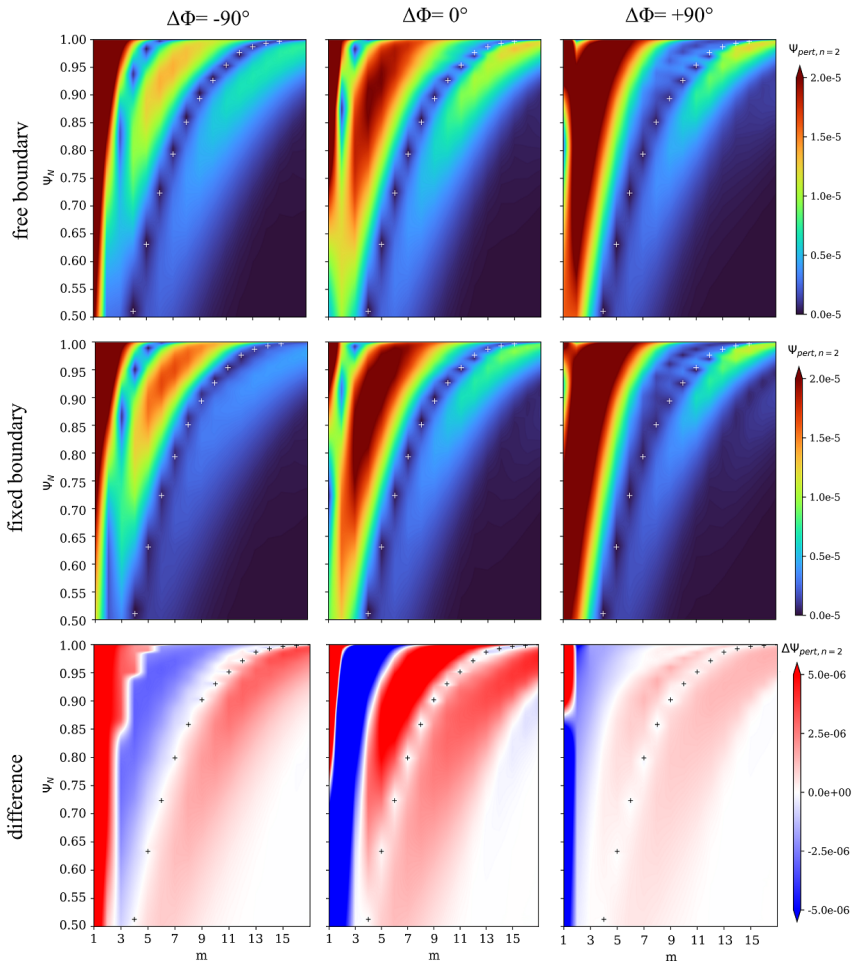

Figure 7.2: Poloidal spectrum of the total perturbed $n = 2$ flux for different coil phases $\Delta\Phi$ calculated with free boundary conditions (top) and fixed boundary conditions (middle). In the bottom row, the difference $\Delta\Phi = \Psi_{\text{pert,n=2,free}} - \Psi_{\text{pert,n=2,fixed}}$ is plotted for each coil phase.

$\Delta\Psi$ shows clearly that the $m+2$ edge kink response is stronger when free boundary conditions are applied. This is confirmed in the radial profile of the kink modes given in figure 7.3.

The edge kink modes can couple to and amplify the pitch aligned components.

However, despite the fact that a stronger edge kink response is observed for all coil phases with free boundary conditions the effects on the pitch aligned components vary. Figure 7.3 shows that when the coils are configured in the $\Delta\Phi = +90°$ coil phase, the difference in the magnitude of the pitch aligned components is very small. In the $\Delta\Phi = 0°$ case the pitch aligned components are smaller with free boundary conditions than with fixed boundary conditions, while the opposite is true of the $\Delta\Phi = -90°$ coil phase.

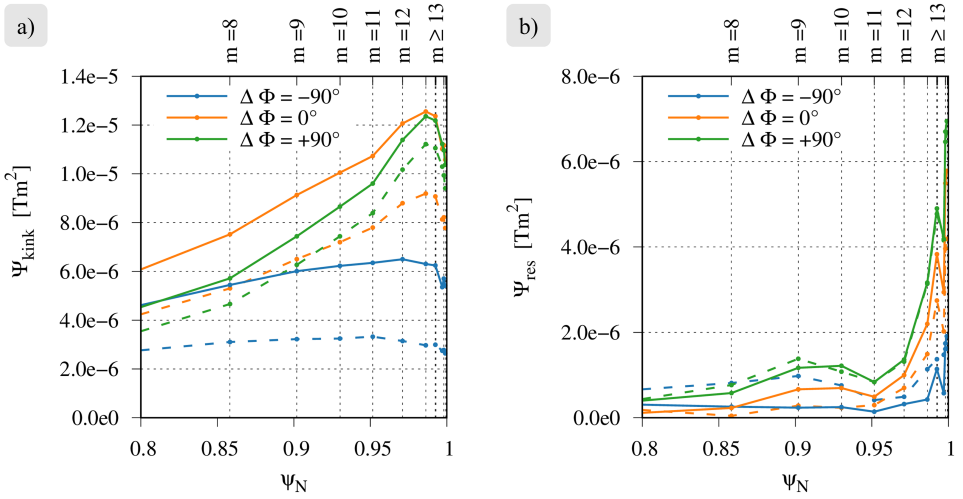

Figure 7.3: (a) The $(m+2, n)$ edge kink component Ψ_{kink} and (b) the (m, n)-pitch aligned component Ψ_{res} on the $q = m/n$ resonant surfaces, calculated with free boundary conditions (solid line) and fixed boundary conditions (dashed lines) for different coil phases $\Delta\Phi$.

A possible explanation for this behavior could be that not only the edge kink response is increased in the free boundary simulation, but also the screening response. The screening response counteracts the amplification of the pitch aligned components by the edge kink response. When fixed boundary conditions are applied, the screening response can not alter the field at the boundary. With this restriction removed at the boundary in the free boundary simulations, the perturbation may be screened below the fixed boundary resonant component. Even if in our sample of coil phases the $\Delta\Phi = 90°$ coil phase still leads to the strongest pitch aligned components, the varying effect of the free boundary could indicate that the ideal coil phase, with the largest pitch aligned components, might be slightly different from that predicted from fixed boundary simulations. In addition, the different amplitudes of kink and screening response could modify the $\boldsymbol{j} \times \boldsymbol{B}$ torque and thus shift the coil current amplitude required for mode penetration and affect the predicted ELM mitigation

or suppression thresholds. However, additional work has to be carried out to further support the validity of these hypotheses.

The variation in the effect of the boundary conditions on the plasma is also reflected in the width of the stochastic layer and island size, demonstrated in the Poincare plots in figure 7.4. When free boundary conditions are applied, the magnetic islands size and stochastic layer width is reduced for the $\Delta\Phi = -90°$ coil phase (a,d), increased for the $\Delta\Phi = 0°$ coil phase (b,e) and unchanged for the $\Delta\Phi = +90°$ coil phase (c,f) compared to the fixed boundary conditions.

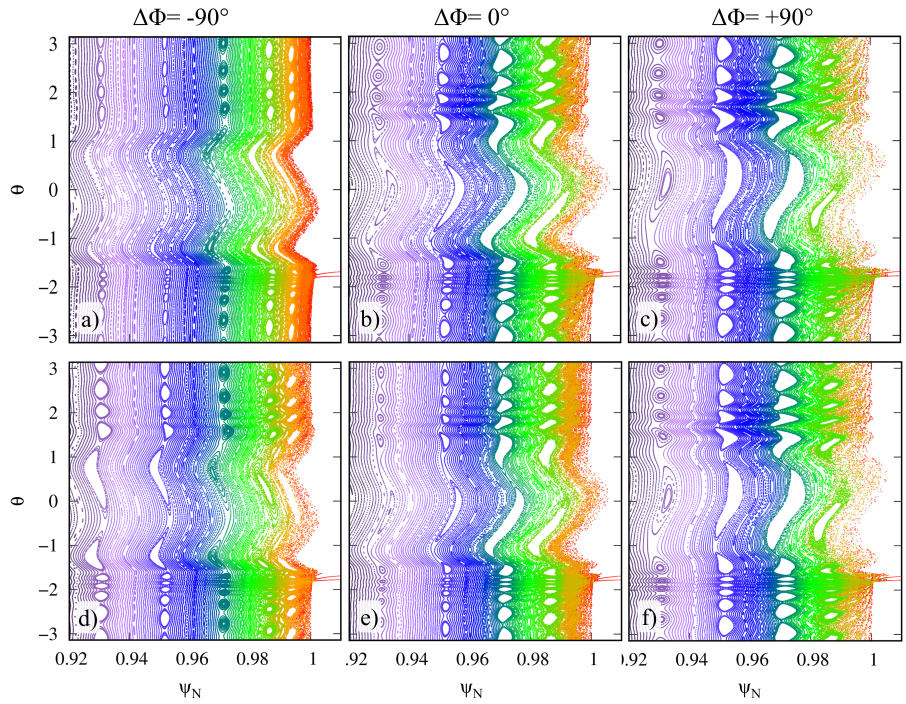

Figure 7.4: (θ, Ψ_N) Poincaré plots for the coil configurations with coil phase $\Delta\Phi$ for the free boundary simulations (a-c) and the fixed boundary simulations (d-f).

In figure 7.5, the comparison to the $v_{\perp,e}$ profile without RMPs is given. For the investigated case with $I_C = 1\,\mathrm{kAt}$, the velocity braking due to RMPs is very small, so that differences between the boundary conditions are practically indistinguishable. Only for the $\Delta\Phi = 0°$ coil phase a slightly stronger velocity braking is observed when free boundary conditions are applied. This could be due to the fact that the increased edge kink response amplifies the resonant component of the perturbation. In turn, slightly stronger mirror currents are induced, which generate a greater $\boldsymbol{j} \times \boldsymbol{B}$ torque. However, this should only be treated as a first preliminary conclusion, as it is based on differences that are very small in comparison to the absolute $v_{\perp,e}$. To

confirm these findings it is necessary to conduct additional studies with coil currents that are closer to the mode penetration threshold.

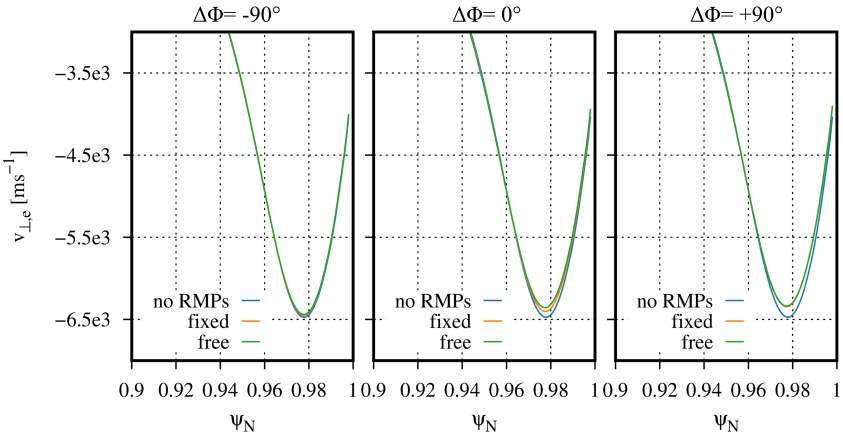

Figure 7.5: The radial profile of the perpendicular electron velocity $v_{\perp,e}$. The RMP coil current of $I_C = 1\,\mathrm{kAt}$ only causes a small reduction of $v_{\perp,e}$, so that the influence of the boundary conditions is barely noticeable for the $\Delta\Phi = -90°$ and $\Delta\Phi = +90°$ coil phase. A slightly stronger velocity braking is observed for the $\Delta\Phi = 0°$ coil phase.

Chapter 8

ELM Simulations with free boundary conditions

After investigating the effect of free boundary conditions on the RMP penetration, the next step is to examine the influence on ELMs and the ELM-RMP interaction. First results of ELM simulations with free boundary conditions are presented in the following. Section 8.1 compares a type-I ELM onset for fixed and free boundary conditions without the application of RMPs. In section 8.2 RMPs are applied to the ELM profile with free boundary conditions, and the differences to the RMP-free case are outlined. A detailed analysis of the results is beyond the scope of this thesis and will be subject to future work.

8.1 Comparison of free boundary and fixed boundary ELM studies

The equilibrium profile used for the RMP penetration studies in the previous chapters is based on the state of an experimental ASDEX Upgrade discharge after an ELM crash taken similarly to [7]. In the following, the same equilibrium will be used to investigate the onset of a type I ELM with both free and fixed boundary conditions. For this purpose, no RMPs are applied and the simulation is continued beyond the time period used in the previous chapters. Since the long computational times of full ELM simulations put them outside the scope of a master thesis, only the ELM onset is studied here.

The time evolution of the magnetic energies of the ELM simulation with fixed boundary conditions is shown in figure 8.3a. Shortly after the non-axisymmetric modes are initialized, the simulation enters a phase with linearly growing magnetic energies. They correspond to resistive peeling-ballooning modes that are destabilized below the ideal peeling-ballooning stability limit. Their peeling-ballooning like structure is illustrated in figure 8.2. At about $t = 2\,\mathrm{ms}$ they are stabilized by the growing E_r-well, which forms together with the growing pedestal due to the increasing pressure gradient. This behavior is also described in [7]. However, due to slight

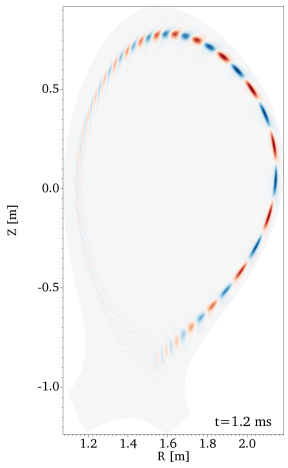

Figure 8.1: The non-axisymmetric temperature components $T_{n>0}$ reveal the peeling-ballooning mode structure of the perturbation.

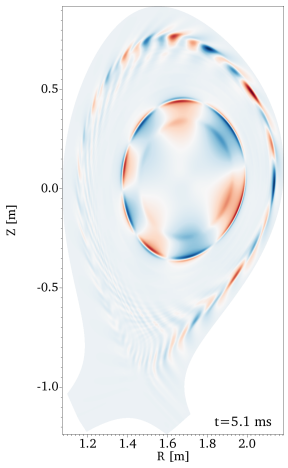

Figure 8.2: As the resistive-peeling ballooning modes begin to stabilize, a $(4, 2)$ mode develops in the core of the plasma.

differences in the resistivity, the modes don't fully stabilize as in [7] and instead a $(4, 2)$ mode develops in the core, which is visible in the poloidal cross section of the temperature in figure 8.2. This mode may alter the plasma dynamics and its development should be avoided in future ELM studies by e.g. adjusting the resistivity. Despite its appearance the basic dynamics of the ELM crash are preserved and the case is suitable for the investigations here.

At $t \approx 5\,\text{ms}$, the $n = 2$ and $n = 6$ modes begin to destabilize. They non-linearly drive the $n = 4$ and high-n modes, whose growth sets in later but steeper. In addition, low frequency oscillations can be seen, especially in the $n = 4$ mode. This type of *precursor activity* is commonly observed before ELM crashes [70, 71]. The precursor phase, with the steadily rising growth rates, terminates in the explosive onset of an ELM. It is marked by a very fast increase in the magnetic energies and followed by a turbulent phase. Due to the strong non-linearity, the simulation of the ELM requires very small times steps, which is why it is terminated a few tenths of a millisecond after the ELM onset in this thesis.

When free boundary conditions are applied, the magnetic energies (figure 8.3b) follow a qualitatively similar evolution. However, the onset of the precursor activity occurs at a far earlier point in the simulation, and the $n = 4$ mode seems to drive the higher n modes. Since the time scale of the precursor activities is smaller, the growth rates are also steeper compared to the fixed boundary case.

The evolution of the magnetic energies suggests that the stability threshold is

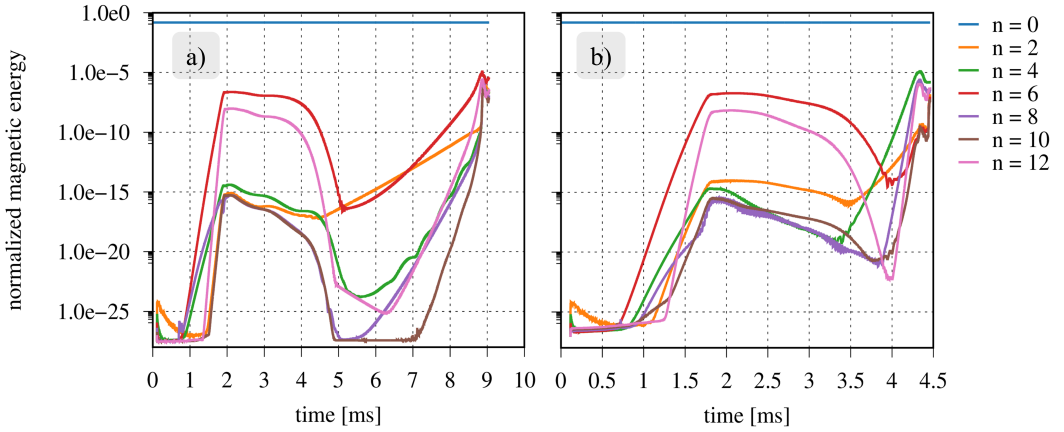

Figure 8.3: The time evolution of the magnetic energies when (a) fixed boundary and (b) free boundary conditions are applied.

crossed earlier in free boundary simulations. The ELM onset occurs at $t \approx 4\,\text{ms}$, instead of $t \approx 9\,\text{ms}$ as with fixed boundary conditions. Right before the free boundary ELM onset the radial profiles of the edge pressure, electron density and potential match the profiles of the fixed boundary simulations. The ELM onset with fixed boundary conditions occurs only when the edge profiles have steepened further due to continuous heating (figure 8.4). This means that the earlier ELM onset can be clearly attributed to the impact of the boundary conditions on the stability limits, rather than an impact on the parameter profiles. It is likely that the modification of the stability limits occurs, because the stabilizing effects of an ideally conducting wall at the JOREK boundary are removed in the free boundary simulations.

The expulsion of heat and particles during the ELM is seen in the drop in the particle and thermal energy content in figure 8.5 and the change in the pedestal profiles in figure 8.6

8.2 Free boundary ELM simulations with RMPs

As final step in this thesis, the free boundary ELM simulations are repeated, this time with the addition of RMPs. The set up is equal to that of the previous chapters, with a coil current of $I_c = 1\,\text{kAt}$ and in the $\Delta\Phi = 90°$ coil configuration. Due to the parameter range of this ELM case, especially the high edge density, RMP-ELM suppression at good plasma confinement is not expected here.

The magnetic energies are shown in figure 8.7. After the RMP ramp up and initial saturation, the growth of instabilities exciting in particular the higher n modes (starting at t=0.7ms) signifies the destabilization of resistive peeling ballooning modes,

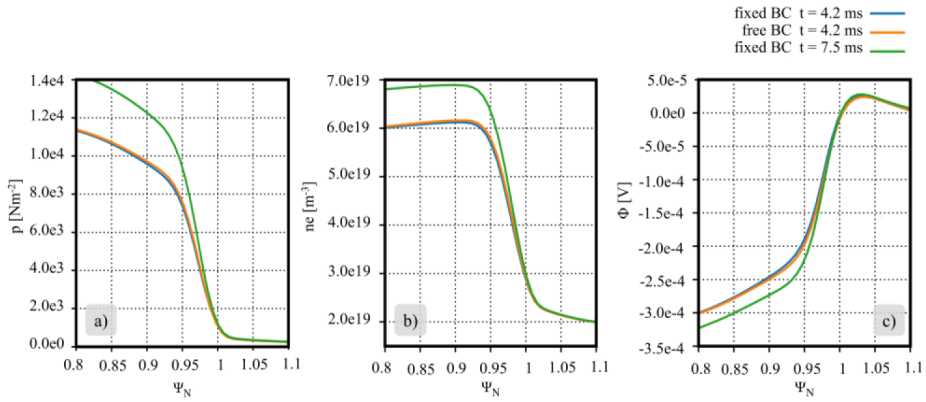

Figure 8.4: Radial profiles of (a) the pressure p, (b) the electron density n_e and (c) the electric potential Φ for the free boundary and the fixed boundary conditions, at $t \approx 4.2\,\text{ms}$, before the ELM onset occurs in the free boundary simulation, and before the onset of the ELM in the fixed boundary simulation at $t \approx 7.5\,\text{ms}$.

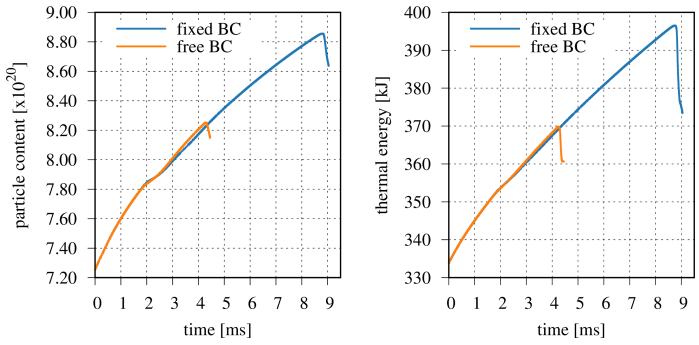

Figure 8.5: The time evolution of the thermal energy and particle content of the ELM simulations with free and fixed boundary.

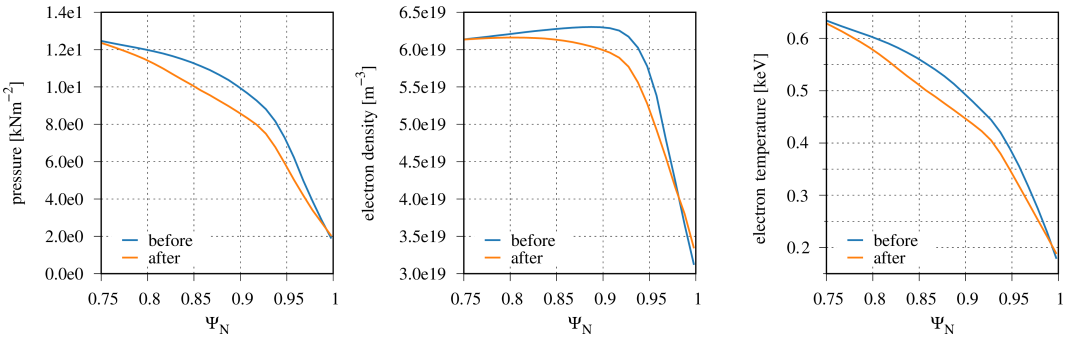

Figure 8.6: Edge profiles of pressure, density and temperature before the ELM onset and after the ELM onset at the end of the simulation.

similarly to the case without RMPs in section 8.1. The oscillations of the magnetic energies correspond to the rotation of magnetic islands in the RMP field. At about $t \approx 0.9\,\mathrm{ms}$ the growth phase then transitions into a non-linear saturation phase, where modes are growing and decaying quickly without a dominating one. In the simulations without RMPs, these modes are stabilized by the growing pedestal. However, when RMPs are applied, the onset of the non-linear phase is correlated with a drop in the edge density and temperature, presumably due to interaction of the resistive peeling-ballooning modes with the RMPs. It keeps the pedestal from forming to the same extent as in the case without RMPs. As a consequence, the peeling-ballooning turbulence is not stabilized, and instead leads to loss of particles and heat, as seen in the lower part of figure 8.7. Between $t \approx 1.4\,\mathrm{ms} - 1.7\,\mathrm{ms}$ the confinement improves and then degrades again. Starting from $t \approx 3\,\mathrm{ms}$, the rapid growth and decay of the individual modes stops and is replaced by saturated modes, with $n = 4$ slightly dominating. A difference in rotation is not observed. It has been found in [7] that a lowered separatrix density may stabilize the resistive peeling-ballooning modes and allow the pedestal to evolve. This could be a possible explanation for the mode saturation and the improvement of the particle confinement from $t = 3\,\mathrm{ms}$ onward. Additional simulation time is needed to confirm this theory.

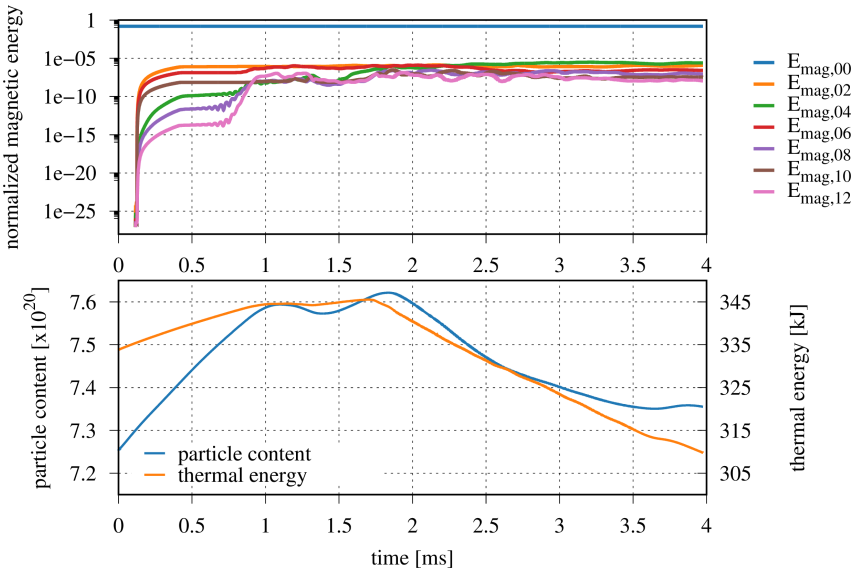

Figure 8.7: (top) Time evolution of the magnetic energies. (bottom) Time evolution of the thermal energy and particle content.

The edge pressure, density and temperature profiles are plotted in figure 8.8 at different points in time, illustrating the profile at the end of the linear mode growth at $t = 0.9\,\mathrm{ms}$, as well as the degraded pedestal during the turbulent phase at $t = 2.4\,\mathrm{ms}$.

The profiles of the simulation without RMPs at the same points in time are given for comparison.

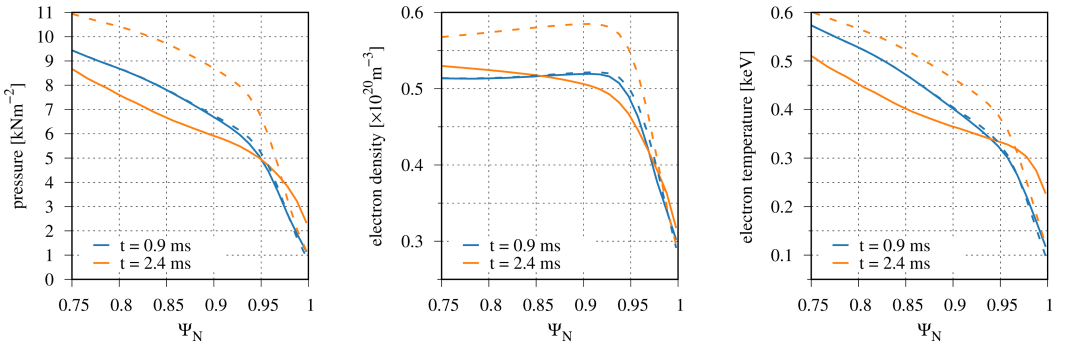

Figure 8.8: Edge pressure, electron density and temperature profiles at the end of the linear growth phase at $t = 0.9\,\mathrm{ms}$ and during the turbulent phase at $t = 2.4\,\mathrm{ms}$

Figure 8.9 shows a time trace of the pressure, electron density and temperature at $\Psi_N = 0.92$ during the non-linear phase of the simulation. It shows that the height of the pedestal oscillates slightly, similar to the small ELM regime described in [7], albeit at a lower frequency and featuring an additional continuous decrease.

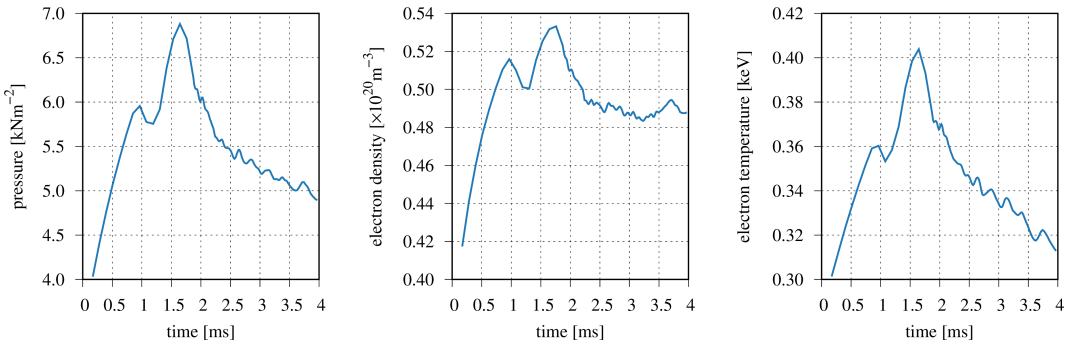

Figure 8.9: Time trace of the edge pressure, electron density and temperature at $\Psi_N = 0.92$ during the non-linear phase.

As mentioned above, this first of a kind simulation of the interaction of RMPs with edge instabilities is not yet done in an experimentally interesting regime and consequently only degraded pedestal confinement is observed. However, it demonstrates the feasibility of such kind of simulations and forms the basis for future studies in different plasma regimes, where experiments show ELM mitigation or suppression at good pedestal confinement. Such simulations are planned and will include scans in plasma parameters and shaping.

Conclusion and outlook

In this thesis simulations of the RMP penetration into ASDEX Upgrade H-Mode plasmas were carried out with JOREK-STARWALL.

Chapter 5 presented the validation of the type of coils, that is used to represent the non-axisymmetric RMP coils in the STARWALL extension of the code. After a correction, the non-axisymmetric coils are fully functional in the code, which was shown by validating their magnetic field at the JOREK computational domain boundary, and by testing the interaction of the active coil with passive conducting structures.

Chapter 6 showed the first results of free boundary RMP simulations with JOREK-STARWALL. It was demonstrated, that the results match the theoretical expectations concerning the plasma response. The effects of RMPs on the plasma, like helical mirror currents, the generation of magnetic island chains and a stochastic layer, or the distortion of the plasma boundary were investigated. The magnitude of the effects was shown to be related to the resonant component of the perturbation, which was varied by applying different coil currents and using different coil configurations.

In Chapter 7 the effect of the free boundary conditions on the penetration of RMPs was determined, by comparison with fixed boundary simulations. The results suggest that the free boundary conditions allow an amplified edge kink response and that the impact on the resonant component is coil configuration dependent.

Finally in Chapter 8 the results of the first ELM-RMP simulations with free boundary conditions were shown. It was demonstrated, that in the absence of RMPs, the ELM onset occurs at lower pedestal gradients, which can be attributed to the absence of the stabilizing ideally conducting wall. The application of RMPs to this case has been demonstrated.

Future work has to be done, to further support the analysis of the effect of free boundary conditions in RMP simulations. In particular, this could include the comparison of a wider range of coil currents, especially closer to the mode penetration threshold. It would be expected that some effects on the plasma are more pronounced near this threshold. In addition, simulations with a better resolved coil phase scan could be performed. This might help to obtain a more precise understanding of the effect of the free boundary on the poloidal spectrum, and in particular the resonant components.

A considerable amount of interesting work has yet to be carried out concerning ELM-RMP simulations with free boundary JOREK-STARWALL. First of all, the

results presented in chapter 8 can be analyzed in more detail, to improve the understanding of the effects of the free boundary. Then, additional simulations can be performed for altered equilibrium parameters. At a lower edge density RMP-ELM suppression is more likely to be observed. Conducting parameter scans would allow to explore the RMP-ELM suppression and mitigation access windows with JOREK-STARWALL.

Overall, the work carried out in this thesis can be seen as a first step towards future improved ELM RMP studies. It builds a solid basis for many upcoming interesting projects, which are likely to provide answers to relevant questions in the field of RMP and ELM physics.

Acknowledgements

First of all, I would like to thank Sibylle Günter for taking the time to supervise the thesis.

Then, I'd like to give special thanks to Matthias Hölzl. This thesis would not have been possible without his support and guidance. Thank you for the encouraging positivity, for pushing me in the right direction and for being available whenever I faced problems.

I am also very thankful for the support I have received from Karl Lackner and the people in the JOREK community, in particular from Nina Schwarz and Javier Artola, who let me benefit immensely from their STARWALL wisdom.

Finally, I am deeply grateful for my family and friends, for providing much needed positive distractions and unconditional support throughout this year.

Bibliography

[1] M. Hoelzl, G. Huijsmans, S. Pamela, M. Becoulet, E. Nardon, F. Artola, B. Nkonga, C. Atanasiu, V. Bandaru, A. Bhole *et al.*, "The JOREK non-linear extended MHD code and applications to large-scale instabilities and their control in magnetically confined fusion plasmas", *arXiv e-prints*, arXiv–2011, 2020.

[2] O. Czarny and G. Huysmans, "Bézier surfaces and finite elements for MHD simulations", *Journal of computational physics*, vol. 227, no. 16, pp. 7423–7445, 2008.

[3] P. Merkel and E. Strumberger, "Linear MHD stability studies with the STARWALL code", *arXiv preprint arXiv:1508.04911*, 2015.

[4] M. Hölzl, P. Merkel, G. Huysmans, E. Nardon, E. Strumberger, R. McAdams, I. Chapman, S. Günter and K. Lackner, "Coupling JOREK and STARWALL codes for non-linear resistive-wall simulations", in *Journal of Physics: Conference Series*, IOP Publishing, vol. 401, 2012, p. 012 010.

[5] G. T. A. Huysmans, S. Pamela, E. van der Plas and P. Ramet, "Non-linear MHD simulations of edge localized modes (ELMs)", *Plasma Physics and Controlled Fusion*, vol. 51, no. 12, p. 124 012, Nov. 2009. DOI: 10.1088/0741-3335/51/12/124012.

[6] M. Hoelzl, G. Huijsmans, F. Orain, F. Artola, S. Pamela, M. Becoulet, D. van Vugt, F. Liu, S. Futatani, A. Lessig, E. Wolfrum, F. Mink, E. Trier, M. Dunne, E. Viezzer, T. Eich, B. Vanovac, L. Frassinetti, S. Guenter, K. Lackner, I. Krebs, A. U. Team and E. M. Team, "Insights into type-I edge localized modes and edge localized mode control from JOREK non-linear magnetohydrodynamic simulations", *Contributions to Plasma Physics*, vol. 58, no. 6-8, pp. 518–528, 2018. DOI: https://doi.org/10.1002/ctpp.201700142.

[7] A. Cathey, M. Hoelzl, K. Lackner, G. Huijsmans, M. Dunne, E. Wolfrum, S. Pamela, F. Orain and S. Günter, "Non-linear extended MHD simulations of type-I edge localised mode cycles in ASDEX Upgrade and their underlying triggering mechanism", *Nuclear Fusion*, vol. 60, no. 12, p. 124 007, Nov. 2020, ISSN: 1741-4326. DOI: 10.1088/1741-4326/abbc87.

[8] E. Nardon, M. Bécoulet, G. Huysmans and O. Czarny, "Magnetohydrodynamics modelling of H-mode plasma response to external resonant magnetic perturbations", *Physics of Plasmas*, vol. 14, no. 9, p. 092 501, 2007.

[9] F. Orain, M. Bécoulet, G. Dif-Pradalier, G. Huijsmans, S. Pamela, E. Nardon, C. Passeron, G. Latu, V. Grandgirard, A. Fil *et al.*, "Non-linear magnetohydrodynamic modeling of plasma response to resonant magnetic perturbations", *Physics of Plasmas*, vol. 20, no. 10, p. 102 510, 2013.

[10] M. Bécoulet, F. Orain, G. T. A. Huijsmans, S. Pamela, P. Cahyna, M. Hoelzl, X. Garbet, E. Franck, E. Sonnendrücker, G. Dif-Pradalier, C. Passeron, G. Latu, J. Morales, E. Nardon, A. Fil, B. Nkonga, A. Ratnani and V. Grandgirard, "Mechanism of Edge Localized Mode Mitigation by Resonant Magnetic Perturbations", *Phys. Rev. Lett.*, vol. 113, p. 115 001, 11 Sep. 2014. DOI: 10.1103/PhysRevLett.113.115001.

[11] F. Orain, M. Bécoulet, J. Morales, G. T. A. Huijsmans, G. Dif-Pradalier, M. Hoelzl, X. Garbet, S. Pamela, E. Nardon, C. Passeron, G. Latu, A. Fil and P. Cahyna, "Non-linear MHD modeling of edge localized mode cycles and mitigation by resonant magnetic perturbations", *Plasma Physics and Controlled Fusion*, vol. 57, no. 1, p. 014 020, Nov. 2014. DOI: 10.1088/0741-3335/57/1/014020.

[12] F. Orain, M. Hoelzl, E. Viezzer, M. Dunne, M. Bécoulet, P. Cahyna, G. Huijsmans, J. Morales, M. Willensdorfer, W. Suttrop *et al.*, "Non-linear modeling of the plasma response to RMPs in ASDEX Upgrade", *Nuclear Fusion*, vol. 57, no. 2, p. 022 013, 2016.

[13] F. Orain, M. Hoelzl, F. Mink, M. Willensdorfer, M. Bécoulet, M. Dunne, S. Günter, G. Huijsmans, K. Lackner, S. Pamela, W. Suttrop and E. Viezzer, "Non-linear modeling of the threshold between ELM mitigation and ELM suppression by resonant magnetic perturbations in ASDEX upgrade", *Physics of Plasmas*, vol. 26, no. 4, p. 042 503, 2019. DOI: 10.1063/1.5091843.

[14] *Iaea endf database*, https://www-nds.iaea.org/exfor/endf.htm, Accessed: 2021-04-13.

[15] J. A. Bittencourt, *Fundamentals of plasma physics*. Springer Science & Business Media, 2013.

[16] J. P. Freidberg, "Ideal magnetohydrodynamic theory of magnetic fusion systems", *Reviews of Modern Physics*, vol. 54, no. 3, p. 801, 1982.

[17] V. Shafranov, "Plasma equilibrium in a magnetic field", *Reviews of plasma physics*, vol. 2, p. 103, 1966.

[18] F. Wagner, G. Becker, K. Behringer, D. Campbell, A. Eberhagen, W. Engelhardt, G. Fussmann, O. Gehre, J. Gernhardt, G. v. Gierke *et al.*, "Regime of improved confinement and high beta in neutral-beam-heated divertor discharges of the ASDEX tokamak", *Physical Review Letters*, vol. 49, no. 19, p. 1408, 1982.

[19] F. Wagner, "A quarter-century of H-mode studies", *Plasma Physics and Controlled Fusion*, vol. 49, no. 12B, B1, 2007.

[20] R. Bickerton, J. Connor and J. Taylor, "Diffusion driven plasma currents and bootstrap tokamak", *Nature Physical Science*, vol. 229, no. 4, pp. 110–112, 1971.

[21] E. Viezzer, "Radial electric field studies in the plasma edge of ASDEX", Feb. 2013. [Online]. Available: http://nbn-resolving.de/urn:nbn:de:bvb:19-161574.

[22] A. E. Lifshits, *Magnetohydrodynamics and spectral theory*. Springer Science & Business Media, 2012, vol. 4.

[23] H. Zohm, "Edge localized modes (ELMs)", *Plasma Physics and Controlled Fusion*, vol. 38, no. 2, pp. 105–128, Feb. 1996. DOI: 10.1088/0741-3335/38/2/001.

[24] J. W. Connor, R. J. Hastie, H. R. Wilson and R. L. Miller, "Magnetohydrodynamic stability of tokamak edge plasmas", *Physics of Plasmas*, vol. 5, no. 7, pp. 2687–2700, 1998. DOI: 10.1063/1.872956.

[25] M. Hölzl, "Diffusive heat transport across magnetic islands and stochastic layers in tokamaks", PhD thesis, Technische Universität München, 2010.

[26] A. Loarte, G. Huijsmans, S. Futatani, L. Baylor, T. Evans, D. Orlov, O. Schmitz, M. Becoulet, P. Cahyna, Y. Gribov *et al.*, "Progress on the application of ELM control schemes to ITER scenarios from the non-active phase to DT operation", *Nuclear Fusion*, vol. 54, no. 3, p. 033 007, 2014.

[27] P. Lang, G. Conway, T. Eich, L. Fattorini, O. Gruber, S. Günter, L. Horton, S. Kalvin, A. Kallenbach, M. Kaufmann *et al.*, "ELM pace making and mitigation by pellet injection in ASDEX Upgrade", *Nuclear Fusion*, vol. 44, no. 5, p. 665, 2004.

[28] P. T. Lang, A. Alonso, B. Alper, E. Belonohy, A. Boboc, S. Devaux, T. Eich, D. Frigione, K. Gál, L. Garzotti *et al.*, "ELM pacing investigations at JET with the new pellet launcher", *Nuclear Fusion*, vol. 51, no. 3, p. 033 010, 2011.

[29] L. Baylor, T. Jernigan, P. Parks, G. Antar, N. Brooks, S. Combs, D. Fehling, C. Foust, W. Houlberg and G. Schmidt, "Comparison of deuterium pellet injection from different locations on the DIII-D tokamak", *Nuclear fusion*, vol. 47, no. 11, p. 1598, 2007.

[30] T. E. Evans, R. A. Moyer, P. R. Thomas, J. G. Watkins, T. H. Osborne, J. A. Boedo, E. J. Doyle, M. E. Fenstermacher, K. H. Finken, R. J. Groebner, M. Groth, J. H. Harris, R. J. La Haye, C. J. Lasnier, S. Masuzaki, N. Ohyabu, D. G. Pretty, T. L. Rhodes, H. Reimerdes, D. L. Rudakov, M. J. Schaffer, G. Wang and L. Zeng, "Suppression of Large Edge-Localized Modes in High-Confinement DIII-D Plasmas with a Stochastic Magnetic Boundary", *Phys. Rev. Lett.*, vol. 92, p. 235 003, 23 Jun. 2004. DOI: 10.1103/PhysRevLett.92.235003.

[31] W. Suttrop, T. Eich, J. C. Fuchs, S. Günter, A. Janzer, A. Herrmann, A. Kallenbach, P. T. Lang, T. Lunt, M. Maraschek, R. M. McDermott, A. Mlynek, T. Pütterich, M. Rott, T. Vierle, E. Wolfrum, Q. Yu, I. Zammuto and H. Zohm, "First Observation of Edge Localized Modes Mitigation with Resonant and Nonresonant Magnetic Perturbations in ASDEX Upgrade", *Phys. Rev. Lett.*, vol. 106, p. 225 004, 22 Jun. 2011. DOI: 10.1103/PhysRevLett.106.225004.

[32] Y. M. Jeon, J.-K. Park, S. W. Yoon, W. H. Ko, S. G. Lee, K. D. Lee, G. S. Yun, Y. U. Nam, W. C. Kim, J.-G. Kwak, K. S. Lee, H. K. Kim and H. L. Yang, "Suppression of Edge Localized Modes in High-Confinement KSTAR Plasmas by Nonaxisymmetric Magnetic Perturbations", *Phys. Rev. Lett.*, vol. 109, p. 035 004, 3 Jul. 2012. DOI: 10.1103/PhysRevLett.109.035004.

[33] Y. Sun, Y. Liang, Y. Q. Liu, S. Gu, X. Yang, W. Guo, T. Shi, M. Jia, L. Wang, B. Lyu, C. Zhou, A. Liu, Q. Zang, H. Liu, N. Chu, H. H. Wang, T. Zhang, J. Qian, L. Xu, K. He, D. Chen, B. Shen, X. Gong, X. Ji, S. Wang, M. Qi, Y. Song, Q. Yuan, Z. Sheng, G. Gao, P. Fu and B. Wan, "Nonlinear Transition from Mitigation to Suppression of the Edge Localized Mode with Resonant Magnetic Perturbations in the EAST Tokamak", *Phys. Rev. Lett.*, vol. 117, p. 115 001, 11 Sep. 2016. DOI: 10.1103/PhysRevLett.117.115001.

[34] Y. Liang, H. R. Koslowski, P. R. Thomas, E. Nardon, B. Alper, P. Andrew, Y. Andrew, G. Arnoux, Y. Baranov, M. Bécoulet, M. Beurskens, T. Biewer, M. Bigi, K. Crombe, E. De La Luna, P. De Vries, W. Fundamenski, S. Gerasimov, C. Giroud, M. P. Gryaznevich, N. Hawkes, S. Hotchin, D. Howell, S. Jachmich, V. Kiptily, L. Moreira, V. Parail, S. D. Pinches, E. Rachlew and O. Zimmermann, "Active control of type-I edge-localized modes with n=1 perturbation fields in the JET tokamak", *Physical Review Letters*, vol. 98, no. 26, 2007.

[35] R. Hawryluk, D. Campbell, G. Janeschitz, P. Thomas, R. Albanese, R. Ambrosino, C. Bachmann, L. Baylor, M. Becoulet, I. Benfatto, J. Bialek, A. Boozer, A. Brooks, R. Budny, T. Casper, M. Cavinato, J.-J. Cordier, V. Chuyanov, E. Doyle, T. Evans, G. Federici, M. Fenstermacher, H. Fujieda, K. G'al, A. Garofalo, L. Garzotti, D. Gates, Y. Gribov, P. Heitzenroeder, T. Hender, N. Holtkamp, D. Humphreys, I. Hutchinson, K. Ioki, J. Johner, G.

Johnson, Y. Kamada, A. Kavin, C. Kessel, R. Khayrutdinov, G. Kramer, A. Kukushkin, K. Lackner, I. Landman, P. Lang, Y. Liang, J. Linke, B. Lipschultz, A. Loarte, G. Loesser, C. Lowry, T. Luce, V. Lukash, S. Maruyama, M. Mattei, J. Menard, M. Merola, A. Mineev, N. Mitchell, E. Nardon, R. Nazikian, B. Nelson, C. Neumeyer, J.-K. Park, R. Pearce, R. Pitts, A. Polevoi, A. Portone, M. Okabayashi, P. Rebut, V. Riccardo, J. Roth, S. Sabbagh, G. Saibene, G. Sannazzaro, M. Schaffer, M. Shimada, A. Sen, A. Sips, C. Skinner, P. Snyder, R. Stambaugh, E. Strait, M. Sugihara, E. Tsitrone, J. Urano, M. Valovic, M. Wade, J. Wesley, R. White, D. Whyte, S. Wu, M. Wykes and L. Zakharov, "Principal physics developments evaluated in the ITER design review", *Nuclear Fusion*, vol. 49, no. 6, p. 065 012, May 2009. DOI: 10.1088/0029-5515/49/6/065012.

[36] W. Suttrop, O. Gruber, S. Günter, D. Hahn, A. Herrmann, M. Rott, T. Vierle, U. Seidel, M. Sempf, B. Streibl, E. Strumberger, D. Yadikin, O. Neubauer, B. Unterberg, E. Gaio, V. Toigo and P. Brunsell, "In-vessel saddle coils for MHD control in ASDEX Upgrade", *Fusion Engineering and Design*, vol. 84, no. 2, pp. 290–294, 2009, Proceeding of the 25th Symposium on Fusion Technology, ISSN: 0920-3796. DOI: https://doi.org/10.1016/j.fusengdes.2008.12.044.

[37] E. Nardon, "Edge localized modes control by resonant magnetic perturbations; Controle des instabilites de bord par perturbations magnetiques resonantes", PhD thesis, 2007.

[38] B. V. Chirikov, "A universal instability of many-dimensional oscillator systems", *Physics Reports*, vol. 52, no. 5, pp. 263–379, 1979, ISSN: 0370-1573. DOI: https://doi.org/10.1016/0370-1573(79)90023-1.

[39] J. Canik, R. Maingi, T. E. Evans, R. Bell, S. Gerhardt, H. Kugel, B. LeBlanc, J. Manickam, J. Menard, T. Osborne *et al.*, "ELM destabilization by externally applied non-axisymmetric magnetic perturbations in NSTX", *Nuclear Fusion*, vol. 50, no. 3, p. 034 012, 2010.

[40] Y. Liang, H. R. Koslowski, P. R. Thomas, E. Nardon, B. Alper, P. Andrew, Y. Andrew, G. Arnoux, Y. Baranov, M. Bécoulet, M. Beurskens, T. Biewer, M. Bigi, K. Crombe, E. De La Luna, P. de Vries, W. Fundamenski, S. Gerasimov, C. Giroud, M. P. Gryaznevich, N. Hawkes, S. Hotchin, D. Howell, S. Jachmich, V. Kiptily, L. Moreira, V. Parail, S. D. Pinches, E. Rachlew and O. Zimmermann, "Active Control of Type-I Edge-Localized Modes with $n = 1$ Perturbation Fields in the JET Tokamak", *Phys. Rev. Lett.*, vol. 98, p. 265 004, 26 Jun. 2007. DOI: 10.1103/PhysRevLett.98.265004.

[41] R. Fitzpatrick, "Bifurcated states of a rotating tokamak plasma in the presence of a static error-field", *Physics of Plasmas*, vol. 5, no. 9, pp. 3325–3341, 1998. DOI: 10.1063/1.873000.

[42] N. Ferraro, "Calculations of two-fluid linear response to non-axisymmetric fields in tokamaks", *Physics of Plasmas*, vol. 19, no. 5, p. 056 105, 2012.

[43] F. Waelbroeck, "Shielding of resonant magnetic perturbations in the long mean-free path regime", *Physics of plasmas*, vol. 10, no. 10, pp. 4040–4047, 2003.

[44] E. Nardon, P. Tamain, M. Bécoulet, G. Huysmans and F. Waelbroeck, "Quasi-linear MHD modelling of H-mode plasma response to resonant magnetic perturbations", *Nuclear Fusion*, vol. 50, no. 3, p. 034 002, 2010.

[45] A. H. Boozer, "Error field amplification and rotation damping in tokamak plasmas", *Physical review letters*, vol. 86, no. 22, p. 5059, 2001.

[46] M. Gryaznevich, T. Hender, D. Howell, C. Challis, H. Koslowski, S. Gerasimov, E. Joffrin, Y. Liu, S. Saarelma, J.-E. contributors *et al.*, "Experimental studies of stability and beta limit in JET", *Plasma Physics and Controlled Fusion*, vol. 50, no. 12, p. 124 030, 2008.

[47] Y. Liu, A. Kirk and E. Nardon, "Full toroidal plasma response to externally applied nonaxisymmetric magnetic fields", *Physics of Plasmas*, vol. 17, no. 12, p. 122 502, 2010. DOI: 10.1063/1.3526677.

[48] A. Kirk, W. Suttrop, I. Chapman, Y. Liu, R. Scannell, A. Thornton, L. B. Orte, P. Cahyna, T. Eich, R. Fischer, C. Fuchs, C. Ham, J. Harrison, M. Jakubowski, B. Kurzan, S. Pamela, M. Peterka, D. Ryan, S. Saarelma, B. Sieglin, M. Valovic, M. Willensdorfer and and, "Effect of resonant magnetic perturbations on low collisionality discharges in MAST and a comparison with ASDEX Upgrade", *Nuclear Fusion*, vol. 55, no. 4, p. 043 011, Mar. 2015. DOI: 10.1088/0029-5515/55/4/043011.

[49] C. Paz-Soldan, R. Nazikian, S. R. Haskey, N. C. Logan, E. J. Strait, N. M. Ferraro, J. M. Hanson, J. D. King, M. J. Lanctot, R. A. Moyer, M. Okabayashi, J.-K. Park, M. W. Shafer and B. J. Tobias, "Observation of a Multimode Plasma Response and its Relationship to Density Pumpout and Edge-Localized Mode Suppression", *Phys. Rev. Lett.*, vol. 114, p. 105 001, 10 Mar. 2015. DOI: 10.1103/PhysRevLett.114.105001.

[50] D. Ryan, Y. Liu, A. Kirk, W. Suttrop, B. Dudson, M. Dunne, R. Fischer, J. Fuchs, M. Garcia-Munoz, B. Kurzan *et al.*, "Toroidal modelling of resonant magnetic perturbations response in ASDEX-Upgrade: coupling between field pitch aligned response and kink amplification", *Plasma Physics and Controlled Fusion*, vol. 57, no. 9, p. 095 008, 2015.

[51] W. Suttrop, A. Kirk, V. Bobkov, M. Cavedon, M. Dunne, R. McDermott, H. Meyer, R. Nazikian, C. Paz-Soldan, D. Ryan, E. Viezzer, M. Willensdorfer and and, "Experimental conditions to suppress edge localised modes by magnetic perturbations in the ASDEX Upgrade tokamak", *Nuclear Fusion*, vol. 58, no. 9, p. 096 031, Jul. 2018. DOI: 10.1088/1741-4326/aace93.

[52] N. Leuthold, W. Suttrop, R. Fischer, A. Kappatou, A. Kirk, R. McDermott, A. Mlynek, M. Valovič, M. Willensdorfer, E. M. Team *et al.*, "Parameter dependence of ELM loss reduction by magnetic perturbations at low pedestal density and collisionality in ASDEX upgrade", *Plasma Physics and Controlled Fusion*, vol. 59, no. 5, p. 055 004, 2017.

[53] T. Evans, M. Fenstermacher, R. Moyer, T. Osborne, J. Watkins, P. Gohil, I. Joseph, M. Schaffer, L. R. Baylor, M. Bécoulet *et al.*, "RMP ELM suppression in DIII-D plasmas with ITER similar shapes and collisionalities", *Nuclear fusion*, vol. 48, no. 2, p. 024 002, 2008.

[54] Q. M. Hu, R. Nazikian, B. A. Grierson, N. C. Logan, D. M. Orlov, C. Paz-Soldan and Q. Yu, "Wide Operational Windows of Edge-Localized Mode Suppression by Resonant Magnetic Perturbations in the DIII-D Tokamak", *Physical Review Letters*, vol. 125, no. 4, Jul. 2020, ISSN: 1079-7114. DOI: 10.1103/physrevlett.125.045001.

[55] T. E. Evans, R. A. Moyer, K. H. Burrell, M. E. Fenstermacher, I. Joseph, A. W. Leonard, T. H. Osborne, G. D. Porter, M. J. Schaffer, P. B. Snyder, P. R. Thomas, J. G. Watkins and W. P. West, "Edge stability and transport control with resonant magnetic perturbations in collisionless tokamak plasmas", *Nature Physics*, vol. 2, no. 6, pp. 419–423, Jun. 2006, ISSN: 1745-2481. DOI: 10.1038/nphys312.

[56] M. Garcia-Munoz, S. Äkäslompolo, P. de Marne, M. G. Dunne, R. Dux, T. E. Evans, N. M. Ferraro, S. Fietz, C. Fuchs, B. Geiger, A. Herrmann, M. Hoelzl, B. Kurzan, N. Lazanyi, R. M. McDermott, M. Nocente, D. C. Pace, M. Rodriguez-Ramos, K. Shinohara, E. Strumberger, W. Suttrop, M. A. V. Zeeland, E. Viezzer, M. Willensdorfer and E. Wolfrum, "Fast-ion losses induced by ELMs and externally applied magnetic perturbations in the ASDEX Upgrade tokamak", *Plasma Physics and Controlled Fusion*, vol. 55, no. 12, p. 124 014, Nov. 2013. DOI: 10.1088/0741-3335/55/12/124014.

[57] Q. Hu, R. Nazikian, B. Grierson, N. Logan, C. Paz-Soldan and Q. Yu, "The role of edge resonant magnetic perturbations in edge-localized-mode suppression and density pump-out in low-collisionality DIII-D plasmas", *Nuclear Fusion*, vol. 60, no. 7, p. 076 001, 2020.

[58] W. Suttrop, A. Kirk, R. Nazikian, N. Leuthold, E. Strumberger, M. Willensdorfer, M. Cavedon, M. Dunne, R. Fischer, S. Fietz, J. C. Fuchs, Y. Q. Liu, R. M. McDermott, F. Orain, D. A. Ryan and E. Viezzer, "Experimental studies of high-confinement mode plasma response to non-axisymmetric magnetic perturbations in ASDEX Upgrade", *Plasma Physics and Controlled Fusion*, vol. 59, no. 1, p. 014 049, Nov. 2016. DOI: 10.1088/0741-3335/59/1/014049.

[59] P. B. Snyder, T. H. Osborne, K. H. Burrell, R. J. Groebner, A. W. Leonard, R. Nazikian, D. M. Orlov, O. Schmitz, M. R. Wade and H. R. Wilson, "The EPED pedestal model and edge localized mode-suppressed regimes: Studies of quiescent H-mode and development of a model for edge localized mode suppression via resonant magnetic perturbations", *Physics of Plasmas*, vol. 19, no. 5, p. 056 115, 2012. DOI: 10.1063/1.3699623.

[60] M. Wade, R. Nazikian, J. deGrassie, T. Evans, N. Ferraro, R. Moyer, D. Orlov, R. Buttery, M. Fenstermacher, A. Garofalo, M. Lanctot, G. McKee, T. Osborne, M. Shafer, W. Solomon, P. Snyder, W. Suttrop, A. Wingen, E. Unterberg and L. Zeng, "Advances in the physics understanding of ELM suppression using resonant magnetic perturbations in DIII-d", *Nuclear Fusion*, vol. 55, no. 2, p. 023 002, Jan. 2015. DOI: 10.1088/0029-5515/55/2/023002.

[61] R. A. Moyer, I. Bykov, D. M. Orlov, T. E. Evans, J. S. Lee, A. M. Teklu, M. E. Fenstermacher, M. Makowski, C. J. Lasnier, H. Q. Wang, J. G. Watkins and W. Wu, "Imaging divertor strike point splitting in RMP ELM suppression experiments in the DIII-D tokamak", *Review of Scientific Instruments*, vol. 89, no. 10, 10E106, 2018. DOI: 10.1063/1.5038350.

[62] I. T. Chapman, A. Kirk, C. J. Ham, J. R. Harrison, Y. Q. Liu, S. Saarelma, R. Scannell, A. J. Thornton, M. Becoulet, F. Orain, W. A. Cooper, S. Pamela and M. Team, "Towards understanding edge localised mode mitigation by resonant magnetic perturbations in MAST", *Physics of Plasmas*, vol. 20, no. 5, p. 056 101, 2013. DOI: 10.1063/1.4801743.

[63] R. Courant, K. Friedrichs and H. Lewy, "Über die partiellen Differenzengleichungen der mathematischen Physik", *Mathematische Annalen*, vol. 100, no. 1, pp. 32–74, Dec. 1928, ISSN: 1432-1807. DOI: 10.1007/BF01448839.

[64] P. J. McCarthy, P. Martin and W. Schneider, "The CLISTE Interpretive Equilibrium Code", eng, Max-Planck-Institut für Plasmaphysik., Garching, Tech. Rep. IPP 5/85, 1999.

[65] E. Nardon, M. Bécoulet, G. Huysmans, O. Czarny, P. Thomas, M. Lipa, R. Moyer, T. Evans, G. Federici, Y. Gribov *et al.*, "Edge localized modes control by resonant magnetic perturbations", *Journal of nuclear materials*, vol. 363, pp. 1071–1075, 2007.

[66] M. Hölzl, P. Merkel, G. T. A. Huysmans, E. Nardon, E. Strumberger, R. McAdams, I. Chapman, S. Günter and K. Lackner, "Coupling JOREK and STARWALL Codes for Non-linear Resistive-wall Simulations", *Journal of Physics: Conference Series*, vol. 401, p. 012 010, Dec. 2012. DOI: 10.1088/1742-6596/401/1/012010.

[67] M. Hoelzl, G. T. A. Huijsmans, P. Merkel, C. Atanasiu, K. Lackner, E. Nardon, K. Aleynikova, F. Liu, E. Strumberger, R. McAdams, I. Chapman and A. Fil, "Non-linear Simulations of MHD Instabilities in Tokamaks Including Eddy Current Effects and Perspectives for the Extension to Halo Currents", *Journal of Physics: Conference Series*, vol. 561, p. 012 011, Nov. 2014. DOI: 10.1088/1742-6596/561/1/012011.

[68] F. Artola, G. Huijsmans, M. Hoelzl, P. Beyer, A. Loarte and Y. Gribov, "Non-linear magnetohydrodynamic simulations of edge localised mode triggering via vertical position oscillations in ITER", *Nuclear Fusion*, vol. 58, no. 9, p. 096 018, 2018.

[69] I. Krebs, F. Artola, C. Sovinec, S. Jardin, K. Bunkers, M. Hoelzl and N. Ferraro, "Axisymmetric simulations of vertical displacement events in tokamaks: A benchmark of M3D-C1, NIMROD, and JOREK", *Physics of Plasmas*, vol. 27, no. 2, p. 022 505, 2020.

[70] T. Kass, S. Günter, M. Maraschek, W. Suttrop, H. Zohm and A. U. Team, "Characteristics of type I and type III ELM precursors in ASDEX upgrade", *Nuclear fusion*, vol. 38, no. 1, p. 111, 1998.

[71] H. Zohm, F. Wagner, M. Endler, J. Gernhardt, E. Holzhauer, W. Kerner and V. Mertens, "Studies of edge localized modes on ASDEX", *Nuclear fusion*, vol. 32, no. 3, p. 489, 1992.